

České vysoké učení technické v Praze
Fakulta jaderná a fyzikálně inženýrská

Katedra fyziky
Experimentální jaderná a částicová fyzika



Měření multiplicity v pp srážkách
v rámci experimentu ALICE během
LHC Run 3

BAKALÁŘSKÁ PRÁCE

Vypracovala: Helena Hesounová
Vedoucí práce: prof. Jesús Guillermo Contreras Nuño Ph.D.
Rok: 2022

Czech Technical University in Prague
Faculty of Nuclear Physics and Physical
Engineering

Department of Physics
Experimental Nuclear and Particle Physics



Multiplicity measurements in pp
collisions with ALICE during the
LHC Run 3

BACHELOR THESIS

Author: Helena Hesounová
Supervisor: prof. Jesús Guillermo Contreras Nuño Ph.D.
Year: 2022



Katedra: fyziky

Akademický rok: 2020/2021

ZADÁNÍ BAKALÁŘSKÉ PRÁCE

Student: Helena Hesounová

Studijní program: Aplikace přírodních věd

Obor: Experimentální jaderná a částicová fyzika

Název práce: Měření multiplicity v pp srážkách v rámci experimentu ALICE během
(česky) LHC Run 3

Název práce: Multiplicity measurements in pp collisions with ALICE during
(anglicky) the LHC Run 3

Pokyny pro vypracování:

1) Vypracování rešerše na téma:

- a) Provedená měření multiplicity v pp srážkách v rámci experimentu ALICE během LHC Run 1 a Run 2
- b) Multiplicita jako nástroj pro měření provázanosti
- c) Upgrade experimentu ALICE pro Run 3

2) Vytvoření simulovaných dat experimentu ALICE pro měření multiplicity v pp srážkách

Doporučená literatura:

- [1] ALICE Collaboration: Technical Design Report for the Muon Forward Tracker, 2015
- [2] ALICE Collaboration: Charged-particle multiplicities in proton-proton collisions at $\sqrt{s} = 0.9$ to 8 TeV, Eur.Phys.J. C77 no.1, 33 (2017)
- [3] Z. Tu, D. E. Kharzeev and T. Ullrich: Einstein-Podolsky-Rosen Paradox and Quantum Entanglement at Subnucleonic Scales, Phys.Rev.Lett. 124 6, 062001 (2020)


Jméno a pracoviště vedoucího bakalářské práce:

prof. Jesus Guillermo Contreras, Ph.D., Katedra fyziky, Fakulta jaderná a fyzikálně inženýrská ČVUT v Praze

Datum zadání bakalářské práce: 23.10.2020

Termín odevzdání bakalářské práce: 07.07.2021

Doba platnosti zadání je dva roky od data zadání.



.....
garant oboru



.....
vedoucí katedry



.....
děkan

V Praze dne 23.10.2020

Prohlášení

Prohlašuji, že jsem svou bakalářskou práci vypracovala samostatně a použila jsem pouze podklady (literaturu, projekty, SW atd.) uvedené v příloženém seznamu.

Nemám závažný důvod proti použití tohoto školního díla ve smyslu § 60 Zákona č. 121/2000 Sb., o právu autorském, o právech souvisejících s právem autorským a o změně některých zákonů (autorský zákon).

V Praze dne

.....

Helena Hesounová

Acknowledgements

I would like to take this opportunity to express my true appreciation of all the help, guidance and support I received from my supervisor prof. Jesús Guillermo Contreras Nuño Ph.D. of the Department of Physics, Faculty of Nuclear Physics and Physical Engineering, Czech Technical University in Prague. I also wish to thank Ing. Tomáš Herman of the Department of Physics, Faculty of Nuclear Physics and Physical Engineering, Czech Technical University in Prague for his advice and technical support.

Helena Hesounová

Název práce:

Měření multiplicity v pp srážkách v rámci experimentu ALICE během LHC Run 3

Autor: Helena Hesounová

Studijní program: Aplikace přírodních věd

Obor: Experimentální jaderná a částicová fyzika

Druh práce: Bakalářská práce

Vedoucí práce: prof. Jesús Guillermo Contreras Nuño Ph.D.

Katedra fyziky, Fakulta jaderná a fyzikálně inženýrská, České vysoké učení technické v Praze

Abstrakt: Na Velkém hadronovém urychlovači (LHC) byl v březnu, po více než tří letech období Long Shutdown 2, spuštěn Run 3. Experiment ALICE v CERNu byl za tuto dobu upgradován. Získal vylepšené detektory a nový software na analýzu dat. Tato vylepšení, mimo jiné výhody, výrazně zvyšují přesnost měření multiplicity a umožňují stálý readout. V září 2021 byly provedeny první testovací runy, které nám poskytly první reálná data upgradovaného experimentu. Tato data slouží ke kalibraci nových detektorů i nového softwaru. Run 505582 proběhl se zápornou polaritou L3 magnetu a run 505673 proběhl s kladnou polaritou tohoto magnetu. Data z těchto dvou runů jsou použita ke kontrole symetrie chování kladně a záporně nabitých částic.

Klíčová slova: LHC, ALICE, multiplicita v pp srážkách

Title:

Multiplicity measurements in pp collisions with ALICE during the LHC Run 3

Author: Helena Hesounová

Study program: Application of Natural Sciences

Specialization: Experimental Nuclear and Particle Physics

Supervisor: prof. Jesús Guillermo Contreras Nuño Ph.D.
Department of Physics, Faculty of Nuclear Physics and Physical Engineering, Czech Technical University in Prague

Abstract: The Large Hadron Collider has started its third Run in April of 2022, after the Long Shutdown 2 period, which lasted more than three years. The ALICE experiment at CERN has upgraded its detectors and its analysis software, during this time, to be capable of continuous readout. These upgrades, among other enhancements, significantly improve the efficiency of multiplicity measurements. A couple of test runs were performed in September 2021 and they provided us with the first set of real data. These data are being used for calibration of all the new features. The run 505582 was done with negative polarity of the L3 magnet and the run 505673 with positive polarity of said magnet. The data from runs with different polarities are used to check the expected symmetry in the behaviour of positively and negatively charged particles.

Key words: LHC, ALICE, multiplicity in pp collisions

Contents

Preface	1
1 Introduction to Particle Physics	3
1.1 The Standard Model	4
1.1.1 Quarks and Leptons	4
1.1.2 Bosons	5
1.1.3 Fundamental Forces	5
1.1.3.1 Gravitational Force	5
1.1.3.2 Electromagnetic force	6
1.1.3.3 Strong Nuclear Force	6
1.1.3.4 Weak Nuclear Force	6
1.2 The Parton Model	6
1.3 Inelastic Scattering	7
1.3.1 Primary Particles	8
1.3.2 Multiplicity	8
1.3.3 Rapidity and Pseudorapidity	8
1.4 Additional Terms	10
1.4.1 Negative Binomial Distribution	10
1.4.2 Beam Gas and Beam Halo Effects	10
2 LHC and ALICE	11
2.1 The Large Hadron Collider	13
2.1.1 The Structure of the LHC	13
2.2 The ALICE experiment	15
2.2.1 ALICE detectors used in Run 2	16
2.2.1.1 Inner Tracking System	16
2.2.1.2 Time Projection Chamber	17
2.2.1.3 Time-of-Flight Detector	17
2.2.1.4 The Forward Region Detectors	18
2.2.2 Upgrade of detectors for the LHC Run 3	18
2.2.2.1 Upgraded Inner Tracking System	19
2.2.2.2 Upgraded Time Projection Chamber	20
2.2.2.3 Fast Interaction Trigger	20
2.2.2.4 Muon Forward Tracker	21
2.2.2.5 Online-Offline system	21
3 Previous related work	25

3.1	Measurements of pp collisions at $\sqrt{s} = 0.9$ TeV	26
3.2	Measurements of pp collisions at $\sqrt{s} = 0.9$ to 8 TeV	28
3.2.1	Track counting algorithms	28
3.2.2	Pseudorapidity densities	28
3.2.2.1	Detector and trigger corrections	29
3.2.2.2	Strangeness corrections	29
3.2.2.3	Event class normalisation	30
3.2.2.4	Experimental results	30
3.2.3	Multiplicity distributions	35
3.2.3.1	Unfolding	35
3.2.3.2	Scaling and fit functions	36
3.2.3.3	Comparison to previous studies	36
3.2.3.4	Comparison to models	37
3.3	Quantum Entanglement	41
3.3.1	Einstein-Podolski-Rosen paradox	41
3.3.2	Testing the presence of quantum entanglement at subnucleonic scales	41
3.3.2.1	Test using simulated data	42
3.3.2.2	Test using experimental data	43
4	Analysis of the first pilot beam data in Run 3	45
4.1	Selection	45
4.2	Reconstructed vertex	46
4.3	Charge of particles	46
4.3.1	φ, η distribution	47
4.4	Transverse momenta	49
4.5	Multiplicity	50
4.6	Comparison with MC simulation	51
	Summary	57

Preface

Modern physics heavily relies on high-energy experiments. The world's largest particle collider, the Large Hadron Collider (LHC), is located at CERN, an international high-energy laboratory straddling the Franco-Swiss border. There are several experiments in the CERN complex, and this thesis uses data from one of them: A Large Ion Collider Experiment (ALICE). ALICE gathers and analyses data on proton-proton or lead-lead collisions and uses them to investigate the current theory of particle physics, the Standard Model. This theory is the main focus of Chapter 1. In addition, the first chapter explains the terminology and principles used in this thesis.

The basic information about the LHC and ALICE (their principle of operation, their structure and their upgrade) is provided in Chapter 2.

Previous measurements of multiplicity in proton-proton collisions and their use in testing the presence of quantum entanglement at subnucleonic scales are discussed in Chapter 3. The first section of this chapter is a summary of measurements of proton-proton collisions at the center-of-mass energy $\sqrt{s} = 0.9$ TeV and is based on [1] published in 2010. The second section is an overview of [2] and it describes the results of measurements of proton-proton collisions at center-of-mass energies from $\sqrt{s} = 0.9$ to 8 TeV. The last section focuses on the quantum entanglement and how to test it using proton-proton collisions.

The last chapter, Chapter 4, contains my contribution to the data analysis of runs 505582 and 505673. The two runs' variables are compared, and the differences between positively and negatively charged particles are explained.

At the end of this thesis is a summary of its contents and results, along with a brief outlook for future studies.

Chapter 1

Introduction to Particle Physics

For centuries, scientists have been trying to find the elementary particles of our Universe. In the occidental world, it all started in ancient Greece with the Atomists. A group of philosophers believed that all matter is composed of atoms, indivisible point-like particles. As time passed, different models of atoms were created and later dismissed, as it became clear that atoms are not elementary.

In 1897 [3], the first subatomic particle, the electron, was discovered by J. J. Thomson. The next particle to be discovered was the proton in 1917, and fifteen years later, in 1932, it was the neutron. The credit for discovering the proton goes to Ernest Rutherford, and for the neutron discovery it goes to James Chadwick.

Once again, scientists believed those particles are elementary, which meant that they do not have an inner structure. However, in the 1960s, physicists Murray Gell-Mann and George Zweig, independently of each other, presented the idea of nucleons, protons and neutrons, having an inner structure. They believed that the nucleons could be composed of new elementary particles called quarks by Gell-Mann. Their existence was investigated in 1968 by experiments with deep-inelastic scattering at the Stanford Linear Accelerator Center. Still, it took several years for the theory to be accepted in the science community. Finally, the constituent quark model was confirmed at the London Conference in 1974 thanks to the explanation of asymptotic freedom using quantum chromodynamics, the theory of the strong interaction [4].

Today, the elementary particles are no longer simple and pointlike because we deal with relativistic quantum fields instead. What we call a particle is the excitation of such a field. A model describing the elementary particles, their behaviour and their interactions, is called the Standard Model, which is the focus of the first section of this chapter, Section 1.1. The parton model is introduced in Section 1.2, and the types of collisions and their parameters are described in Section 1.3. Lastly, some additional terms are explained in Section 1.4.

1.1 The Standard Model

There are many elementary particles known today. The Standard Model divides them into four groups: quarks, leptons, gauge bosons and scalar bosons. There are six quarks, and for each of them, there is an antiquark. The same thing applies to leptons. Quarks and leptons are the bricks of matter. The gauge bosons are the intermediate particles of the four fundamental forces. Lastly, there is one scalar boson called the Higgs boson.

However, there are other types of groups into which we can divide elementary and compound particles using different criteria. For instance, we can divide all particles into two groups by their spin. Spin is an inner angular momentum. It is an observable used only in quantum mechanics and has no parallel in classical physics. It can have an integer or half-integer value and so particles can be divided into two groups by that. Particles with half-integer spin are called fermions and particles with integer spin are called bosons.

Standard Model of Elementary Particles

		three generations of matter (elementary fermions)			three generations of antimatter (elementary antifermions)			interactions / force carriers (elementary bosons)	
		I	II	III	I	II	III		
mass	$\approx 2.2 \text{ MeV}/c^2$	$\approx 1.28 \text{ GeV}/c^2$	$\approx 173.1 \text{ GeV}/c^2$	$\approx 2.2 \text{ MeV}/c^2$	$\approx 1.28 \text{ GeV}/c^2$	$\approx 173.1 \text{ GeV}/c^2$	0	0	$\approx 124.97 \text{ GeV}/c^2$
charge	$\frac{2}{3}$	$\frac{2}{3}$	$\frac{2}{3}$	$-\frac{2}{3}$	$-\frac{2}{3}$	$-\frac{2}{3}$	0	0	0
spin	$\frac{1}{2}$	$\frac{1}{2}$	$\frac{1}{2}$	$\frac{1}{2}$	$\frac{1}{2}$	$\frac{1}{2}$	1	0	0
	u	c	t	ū	ĉ	t̄	g	H	
	up	charm	top	antiup	anticharm	antitop	gluon	higgs	
QUARKS	$\approx 4.7 \text{ MeV}/c^2$	$\approx 96 \text{ MeV}/c^2$	$\approx 4.18 \text{ GeV}/c^2$	$\approx 4.7 \text{ MeV}/c^2$	$\approx 96 \text{ MeV}/c^2$	$\approx 4.18 \text{ GeV}/c^2$	0	0	
	$-\frac{1}{3}$	$-\frac{1}{3}$	$\frac{1}{3}$	$-\frac{1}{3}$	$-\frac{1}{3}$	$\frac{1}{3}$	0	0	
	$\frac{1}{2}$	$\frac{1}{2}$	$\frac{1}{2}$	$\frac{1}{2}$	$\frac{1}{2}$	$\frac{1}{2}$	1	1	
	d	s	b	d̄	ṡ	b̄	γ	Z	
	down	strange	bottom	antidown	antistrange	antibottom	photon	Z⁰ boson	
LEPTONS	$\approx 0.511 \text{ MeV}/c^2$	$\approx 105.66 \text{ MeV}/c^2$	$\approx 1.7768 \text{ GeV}/c^2$	$\approx 0.511 \text{ MeV}/c^2$	$\approx 105.66 \text{ MeV}/c^2$	$\approx 1.7768 \text{ GeV}/c^2$	$\approx 91.19 \text{ GeV}/c^2$	0	
	-1	-1	$\frac{1}{2}$	1	1	1	1	0	
	$\frac{1}{2}$	$\frac{1}{2}$	$\frac{1}{2}$	$\frac{1}{2}$	$\frac{1}{2}$	$\frac{1}{2}$	1	1	
	e	μ	τ	e⁺	μ̄	τ̄	Z⁰ boson	Z⁰ boson	
	electron	muon	tau	positron	antimuon	antitau	Z⁰ boson	Z⁰ boson	
	$< 2.2 \text{ eV}/c^2$	$< 0.17 \text{ MeV}/c^2$	$< 18.2 \text{ MeV}/c^2$	$< 2.2 \text{ eV}/c^2$	$< 0.17 \text{ MeV}/c^2$	$< 18.2 \text{ MeV}/c^2$	$\approx 80.39 \text{ GeV}/c^2$	1	
	0	0	0	0	0	0	1	1	
	$\frac{1}{2}$	$\frac{1}{2}$	$\frac{1}{2}$	$\frac{1}{2}$	$\frac{1}{2}$	$\frac{1}{2}$	1	1	
	ν_e	ν_μ	ν_τ	ν̄_e	ν̄_μ	ν̄_τ	W⁺	W⁻	
	electron neutrino	muon neutrino	tau neutrino	electron antineutrino	muon antineutrino	tau antineutrino	W⁺ boson	W⁻ boson	

Figure 1.1: Table of elementary particles including antiparticles according to the Standard Model. Taken from [5].

Elementary fermions are leptons and quarks. Nonelementary fermions are called baryons. Baryons are particles composed of three quarks or antiquarks, but those are called antibaryons. Elementary bosons are gauge, and scalar bosons and nonelementary bosons are called mesons. Mesons are particles containing one quark and one antiquark. Mesons and baryons are together called hadrons.

1.1.1 Quarks and Leptons

Both quarks and leptons exist in three generations, and generations differ in the rest mass.

The first generation of quarks contains up and down quarks that make up protons and neutrons. The second generation includes charm and strange quarks. Strange quarks sometimes appear in a nucleus, making it a hypernucleus. Charm quarks may also appear in some nuclei, but this has not been observed yet. The last generation contains top and bottom, also called beauty, quarks, which are very heavy. The top quark is, in fact, so heavy that it does not exist in a bound state.

Each lepton generation contains a negatively charged particle, electron, muon or tau, and a very light neutral particle called a neutrino. There are three types of neutrinos: electron, muon and tau neutrinos.

1.1.2 Bosons

All elementary gauge bosons are intermediate particles of the fundamental forces. The Higgs boson is the excitation of the Higgs field, which is responsible for the rest mass of all elementary particles. The photon is the mediator of the electromagnetic force; gluons are intermediate particles of the strong nuclear force, and the Z^0 and W^\pm bosons are mediators of the weak nuclear force. The one mediator, which is not in the Fig. 1.1, is the graviton, as it has not yet been proved that it truly exists. Moreover, gravity, the fourth fundamental force of the Universe, has not been included in the Standard Model as it has not been unified with the other fundamental forces. A theory, eagerly awaited for a hundred years, that would include all fundamental forces is called the Theory of Everything.

1.1.3 Fundamental Forces

Even though the Standard Model describes quite well the nuclear forces and the electromagnetic force, it does not mean it is the unified theory of all those three forces. Electric and magnetic fields were united together by Maxwell in the 1860s, and the electromagnetic force was united with the weak force into an electroweak force a hundred years later. The theory that would truly unify electroweak and strong forces is called the Grand Unification Theory.

1.1.3.1 Gravitational Force

The gravitational force is very strong when looking at the big picture. Moreover, it has an infinite range, and it acts on the energy-momentum of any field, regardless of the charge of particles or any other properties. However, it is absolutely negligible compared to the nuclear and electromagnetic forces on the scales of nucleons or even atoms. Its relative strength is $\alpha_G \approx 10^{-39}$. Because of that, the gravitational force is not discussed in this thesis at all.

1.1.3.2 Electromagnetic force

The electromagnetic force, mediated by massless photons, affects only electrically charged particles, and its relative strength is $\alpha_{EM} = \frac{1}{137}$. This force is responsible for binding the electrons to the nucleus, creating atoms. It also creates all the chemical bonds between atoms. Another effect of this force is the Coulombic repulsion of protons in a nucleus.

The response of a charged particle to the electromagnetic field is dependent on its charge and momentum, which is crucial for detection. A charged particle traveling through a magnetic field will have a curved trajectory. The direction of the curving depends on the positivity or negativity of the charge, whereas the curvature is dependent on the particle's momentum; the lower the momentum, the bigger the curvature.

1.1.3.3 Strong Nuclear Force

The strong nuclear force is mediated by gluons and affects only particles with the colour charge. Those particles are quarks and gluons. The strong force binds quarks together, creating nucleons, and its residues binds the nucleons together, creating a nucleus. Unlike photons, which cannot interact with each other, gluon-gluon interactions are quite common. The range of this force is very small, about 10^{-15} m and it shows saturation. Saturation results in a more or less constant binding energy per nucleon. The relative strength is $\alpha_S \approx 1$.

1.1.3.4 Weak Nuclear Force

The weak nuclear force, mediated by the Z^0 , W^\pm bosons, has a relative strength of $\alpha_W = 10^{-7}$ and a range of only about 10^{-17} m. However, the low strength and low range do not mean this force is negligible in particle physics, as it is the only force allowing the breaking of certain symmetries and laws of conservation. This results in radioactive beta decay. In addition, the weak nuclear force acts on particles with a weak charge. Those particles are, for example, quarks, leptons, neutrinos etc.

1.2 The Parton Model

The parton model is a model of a nucleus created by Richard Feynman in 1969 and presented by him at CERN in 1970. It stands on an idea of a nucleus composed of smaller particles called partons. There is no connection between partons and quarks in their definition, as there are no initial assumptions about the partons. Their nature is determined solely by experiments.

If we apply this model to a collision of two protons, we can say that the interaction happens between two partons, each from a different nucleon, and that these partons

are independent of the rest of the nucleons. This simplifies the matter as the partons are considered point-like.

The partons are identified with quarks and gluons. The parton model takes into consideration also the virtual particles that may appear in the nucleus. Virtual particles are quantum fluctuations allowed by the Heisenberg's uncertainty principle:

$$\Delta E \Delta t \geq \frac{\hbar}{2}. \quad (1.1)$$

As they are bound by the inequality, they have a very limited lifetime and energy, but they can exist and interact.

Each parton carries a part of the nucleon's momentum; that part is usually denoted by x , which is the fraction of the parton's momentum over the nucleon's momentum.

1.3 Inelastic Scattering

When particles of any sort collide, there are two possible ways how the scattering can happen. Either the particles bounce off of each other and stay the same; this is called elastic scattering. Or the particles collide, excite and fragment; in that case, it is an inelastic scattering.

In this thesis, the main studied variable is multiplicity. Multiplicity is the number of particles created by the collision. In elastic scattering, no new particles are created; therefore, in this thesis, only inelastic events are analysed.

Inelastic events can be further divided based on diffraction. Diffractive events are when the interaction between two particles is mediated by a colourless pomeron, which creates a large rapidity (and pseudorapidity) gap between the produced particles. Usually, we distinguish double or single diffractive events because central diffraction has a low probability and is difficult to recognise as it is very similar to classical inelastic events. Double diffraction means both particles, in our case protons, fragment and create new particles, which travel close to the direction of the incoming protons. Single diffraction is the case when one proton fragments and one does not.

In ALICE studies, there are three event classes investigated: INEL, NSD and INEL>0. INEL class contains all inelastic events detected, NSD (non-single diffractive) class contains all but the single diffractive events and the INEL>0 class contains all inelastic events with at least one primary charged particle in the pseudorapidity range smaller than 1.

Another variable that we can use to divide collisions into groups is the momentum transfer. If the momentum transferred in a collision is small, the process is called soft, but if it is large, the event is called a hard scattering. A problem arises when both these types of collisions appear in the same set of events because each of them involves different aspects of the theory of the strong interaction called quantum chromodynamics (QCD). This makes the total cross section difficult to calculate.

Cross section is a variable describing the probability of an occurrence of a specific process under specific conditions.

1.3.1 Primary Particles

In inelastic events, many particles are created and later detected. Those particles are called primary particles. However, some of the particles created by the collision later decay because of the weak force. Those particles are called secondary particles. The particles created due to an interaction with a detector are also called secondary.

Secondary particles can be recognised because their vertex is not the same as the primary vertex of the collision. The collision vertex is the crossing point of reconstructed tracks. It is determined with precision high enough that the secondary vertexes of the weak decays are visibly different.

The distance between primary and secondary vertexes is given by the fact that a weak decay is a slow process. It gives the particle enough time to travel some distance before decaying. Unlike that, the strong decays happen so quickly that the vertex of this decay is indistinguishable from the primary one. So the products of strong decays are still called primary particles.

1.3.2 Multiplicity

As stated before, multiplicity is an observable describing the number of particles created by a collision. It is usually the first variable measured and discussed as it is easier to measure than most other observables. The only thing needed to determine an event's multiplicity is the number of reconstructed tracks. There is no need for particle identification or measurements of particles momenta.

In addition, multiplicity is a good variable for a comparison of different collisions. Its distribution of all the events analysed is smooth and easily compared. It is usually plotted as a histogram of the number of events with the given multiplicity, but it can be redone as a probability distribution.

1.3.3 Rapidity and Pseudorapidity

Another critical variable in accelerator physics is rapidity, or pseudorapidity. Before defining these two variables, specifying the Lorentz transformation and defining the transversal momentum is needed.

The frame used to describe the collision is often taken as z axis being the beam axis. That means the Lorentz boost is with respect to the z axis. Therefore, for the 4-momentum in the laboratory frame applies:

$$\begin{aligned}
E'/c &= \gamma(E/c - \beta p_z), \\
p'_x &= p_x, \\
p'_y &= p_y, \\
p'_z &= \gamma(p_z - \beta E/c).
\end{aligned}$$

As the x and y components are Lorentz invariant, they are usually put together as $\vec{p}_T = \vec{p}_\perp$ called the transversal momentum.

Now, the definition of rapidity is:

$$y = \frac{1}{2} \ln \left(\frac{E + p_z c}{E - p_z c} \right). \quad (1.2)$$

This variable is zero for particles with direction perpendicular to the beam axis and goes to infinity or minus infinity for particles going in the beam axis directions. So it can be used to describe the particle's direction. But this variable is not Lorentz invariant and it transforms as:

$$y' = y + \ln \sqrt{\frac{1 - \beta}{1 + \beta}} = y - \tanh^{-1} \beta. \quad (1.3)$$

From this relation, it is evident that the difference between the rapidities of the two particles remains the same after the Lorentz transformation. So, even though the rapidity itself is not Lorentz invariant, the difference of the two rapidities is.

However, there is a problem with rapidity for highly relativistic particles. To calculate the rapidity, it is necessary to know the total energy and momentum of a particle, which is very difficult to obtain. A new variable, similar to rapidity, is defined to avoid this problem. Pseudorapidity is an approximation of rapidity, where the particle's mass is neglected. Therefore, for highly relativistic particles, where the mass is negligible compared to the momentum, these two variables are very close. Pseudorapidity is defined as:

$$\eta = - \ln \tan \frac{\theta}{2}, \quad (1.4)$$

where θ is the angle between the beam axis and the particle's trajectory, it is also zero for perpendicular directions and $\pm\infty$ for directions parallel to the z axis.

An often used observable is the pseudorapidity density, which is defined as $\langle dN_{\text{ch}}/d\eta \rangle$, where N_{ch} is the number of charged particles (multiplicity) and η is pseudorapidity. It is usually plotted against energy or pseudorapidity.

1.4 Additional Terms

In this thesis, some additional terms are being used, and this section is dedicated to their explanation. The terms described here are negative binomial distribution (NBD), beam gas, and beam halo effects.

1.4.1 Negative Binomial Distribution

The negative binomial distribution (NBD) is a discrete probability distribution. It is a model of the number of successful events that happen before a specific number of failed events is reached. The events are so-called Bernoulli or binomial trials, hence the name. A binomial trial means exactly two possible outcomes of a random experiment.

The NBD distribution can also be considered a generalisation of the Poisson probability, where the variance depends on two parameters. In studies of multiplicities, this is the commonly used interpretation.

1.4.2 Beam Gas and Beam Halo Effects

The vacuum in the tubes of accelerators is extremely high, but it is not perfect. As a result, there are residues of the gas and residues from the collisions, which sometimes travel along the beam itself, creating a beam halo. Therefore, some of the collisions detected by experiments are not collisions of the particles expected but of the residual particles.

These collisions are a nuisance, they create noise in collected signals, and they make it more difficult to extract a clean signal from the detectors. So, one of the aims of an analysis is then to remove as many of these events as possible from the data.

Chapter 2

LHC and ALICE

This chapter provides basic information about the CERN complex, the LHC and the ALICE experiment. The principle of operation of the Large Hadron Collider is explained in Section 2.1, and the structure and upgrade of ALICE are described in Section 2.2.

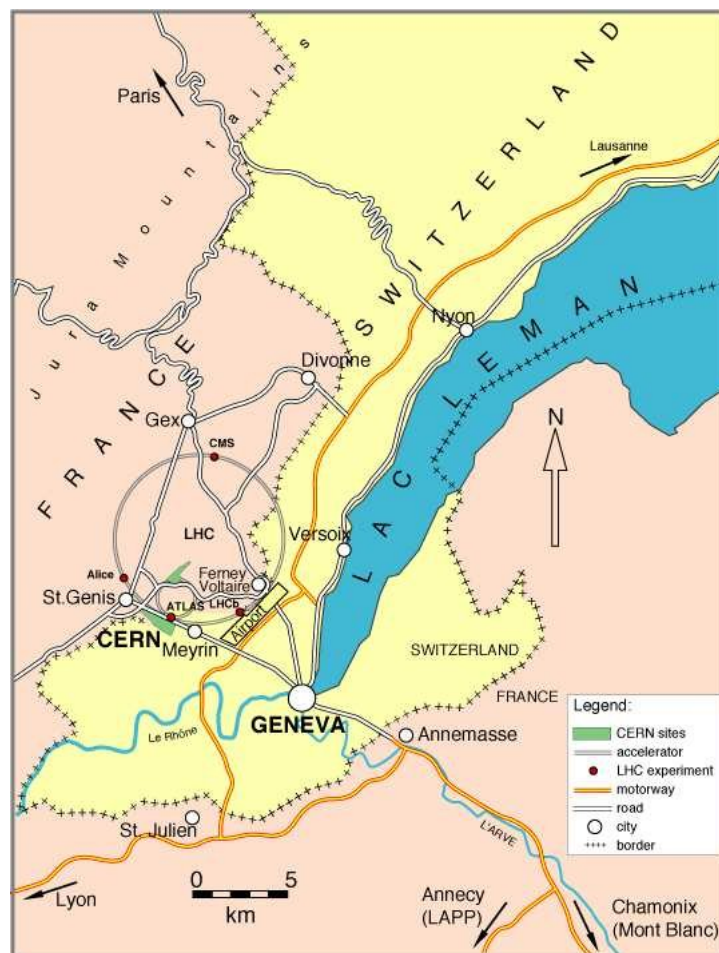


Figure 2.1: The location of the CERN acceleration complex. Taken from [6].

ALICE is an acronym for A Large Ion Collider Experiment, a complex of detectors at the LHC. The LHC, Large Hadron Collider, is currently the most powerful particle accelerator in the world. It is part of the CERN's accelerator complex on the Franco-Swiss border close to Geneva. The exact location of the CERN complex is shown in Fig. 2.1.

CERN, the European Organization for Nuclear Research, was established in 1954 by twelve founding states: Belgium, Denmark, France, the Federal Republic of Germany, Greece, Italy, the Netherlands, Norway, Sweden, Switzerland, the United Kingdom, and Yugoslavia. Its purpose was to bring European countries together after World War II and stop European scientists from leaving and going to the USA.

The convention was signed in 1953, and it stated that: "The Organization shall have no concern with work for military requirements and the results of its experimental and theoretical work shall be published or otherwise made generally available" [7]. Throughout history, up to this day, the organization has stayed true to this proclamation. In the convention the acronym CERN was used for the first time and it was short for Conseil Européen pour la Recherche Nucléaire. This name is not used anymore, but the acronym CERN stayed.

Today the international collaboration at CERN unites more than 110 nationalities and more than 70 countries, of which 23, including the Czech Republic, are the so-called Member States. Membership grants the countries special privileges and duties.

CERN's mission has always been to study the fundamental physics of the universe, develop new technologies and educate and train new generations of scientists and engineers.

One of the biggest achievements at the LHC, regarding the Standard Model, was the discovery of the Higgs boson in 2012. However, the most practical invention coming from CERN remains the World Wide Web (WWW), invented by a British scientist, Tim Berners-Lee, in 1989.

2.1 The Large Hadron Collider

The Large Hadron Collider is the most recent addition to the accelerator complex of CERN. The construction started in the 2000s, but the idea was around from the 1980s [8]. In 2008 the new accelerator provided its first data.

The whole complex works in LHC Runs. An LHC Run usually lasts approximately three years and is followed by a two-year gap called Long Shutdown (LS). During the shutdown, the accelerator and the experiments get repaired and upgraded.

The LHC Run 1 took place from 2009 to 2013. The proton beams reached a maximum energy of 4 TeV. During this run, the Higgs boson was observed. For the next two years, the LHC was being repaired, so it could reach the expected energy of 14 TeV for proton-proton collisions.

The LHC Run 2 started in the summer of 2015 and ended at the beginning of 2019 with the next shutdown, the LS2. During this run, a lot of data for proton-proton collisions have been acquired by ALICE, and the results on multiplicity published at the beginning of 2017 are the focus of Section 3.2.

During the year 2021, the last upgrade was finished, and the first data of LHC Run 3, called pilot-beam collisions, were produced. These data are only from the test run; therefore they regard only proton-proton collisions at the injection energy of 0.9 TeV. These data are analysed in Chapter 4.

2.1.1 The Structure of the LHC

The LHC is located inside a 27 km long circular tunnel in average 100 m underground. In that tunnel, two high-energy particle beams travel at ultra-relativistic velocities in opposite directions. Each beam has a separate tube at ultrahigh vacuum (10^{-13} bar, which is a ten times lower pressure than in outer space), and the particles are kept on their circular trajectory using superconducting electromagnets. To reach the superconducting state, the electromagnets are cooled to 1.9 K, a temperature lower than the one in the outer space.

Before entering the LHC, particles are firstly accelerated within the older complex for 10 min until they reach the required energy of 450 GeV. The schema of the complex is in Fig. 2.2.

As the source of protons, a bottle of hydrogen gas is used. Those protons are firstly injected into the Linac 2 tube, which accelerates them to an energy of 50 MeV. From there, they are injected into the Proton Synchrotron Booster (PSB), where the beam reaches energy of 1.4 GeV, and it is accumulated into bunches. Nextly, those bunches enter the Proton Synchrotron (PS), which they leave with the energy of 25 GeV. The next part of the chain is the Super Proton Synchrotron (SPS), where the protons reach 450 GeV. That is their injection energy at which they enter the LHC. The filling of the tubes takes less than 5 min and an additional 20 min are needed to reach the energy wanted for colliding. After their injection and acceleration in the LHC tubes, the beams circulate and collide for several hours. Each beam is composed of

bunches containing approximately 10^{11} protons for proton-proton collisions. When approaching a crossing, a magnetic field is used to reduce the radius of each beam to increase the collision's probability; this process is called focustion.

CERN's Accelerator Complex

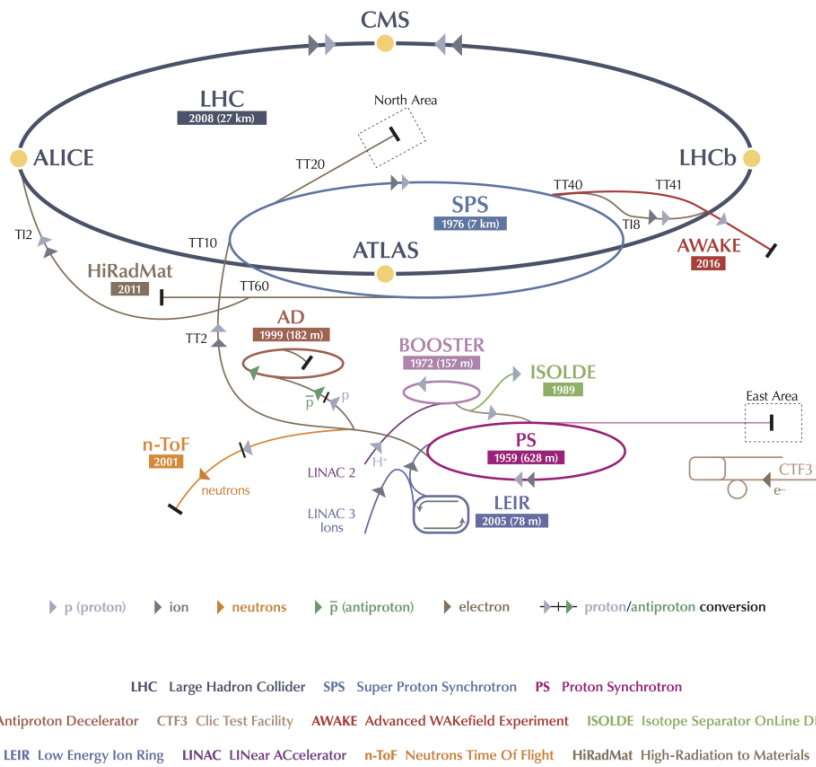


Figure 2.2: The schema of the CERN acceleration complex. Taken from [9].

2.2 The ALICE experiment

At the LHC, there are four places where the beams cross, and there is an experiment at each one of them. There are LHCb, ATLAS, CMS and the focus of this thesis, ALICE. The main mission of ALICE is to study high-energy collisions of protons or heavy nuclei, mostly lead. It observes the creation of particles that follows the cooling phase of the quark-gluon plasma (QGP) created by the collision.

As an information source for this chapter, the ALICE collaboration web page was used [10].

The 10000 t detector is a 26 m long cylinder with a diameter of 16 m placed 56 m under ground. The ALICE Collaboration consists of more than a thousand scientists from 30 countries [11].

The cylinder is filled with many complex detectors to determine as many properties of the events as possible. The experiment consists of the Inner Tracking System (ITS), the Time Projection Chamber (TPC), the Time-of-Flight (TOF) detector, the Forward Multiplicity Detector (FMD) and others. The whole complex was upgraded during the last Long Shutdown (LS2). During that time, new software for the data acquisition process, called the Online-Offline system, was created.

When reconstructing an event, one of the most important pieces of information to characterize it is its centrality, which is a proxy for the impact parameter of the collision, usually denoted by b . This is measured by the Zero Degree Calorimeters (ZDCs) placed approximately 110 m from the collision vertex along the beamline, on both sides, with additional information about the number and spatial distribution of particles produced from the Forward Interaction Trigger, which is the successor of the Forward Multiplicity Detector (FMD) and the V0 and T0 detectors. T0 also served as a trigger as it measured the time of the event with high precision. Its successor also has this feature.

Another piece of information needed to reconstruct an event properly is the position of the event vertex. This helps to distinguish primary particles created by the collision itself from particles created by later decays. The vertex position is determined from reconstructed tracks of detected particles. The ITS, TPC, TOF, and the Transition Radiation Detector (TRD) are used for tracking particles. From the hits detected by these detectors, the trajectories of particles are reconstructed. These detectors are placed in a magnetic field created by a solenoid magnet, the so-called L3. This causes bending of the particle trajectories from which we can determine their charge and momentum. The precision of the primary vertex reconstruction is within 100 μm . This allows us to recognise particles created by weak decays. For the LHC Run 3, the ITS will be completely new, allowing ALICE to improve the precision of the primary vertex reconstruction.

Other detectors are used to determine the identity of particles. The TOF detector measures the time a particle needs to travel from the primary vertex to the detector with a precision of 0.1 ns; this allows us to determine the velocity of particles with high precision. The TRD is used to identify electrons from their radiation while crossing different materials. Muons are detected by the muon spectrometer and

newly by the Muon Forward Tracker (MFT).

2.2.1 ALICE detectors used in Run 2

Before the upgrade during LS2, the ALICE experiment had a structure, which can be seen in Fig. 2.3. There was a central barrel surrounded by a huge solenoid magnet (9) and detectors in the forward and backward regions. The central barrel consisted of the Inner Tracking system ITS (1), the Time Projection Chamber TPC (2), the Transition Radiation Detector TRD (4), the Time-of-flight detector TOF (5) and HMPID (a Cherenkov detector) (6) and two electromagnetic calorimeters PHOS (7) and EMCal (8). In the forward and backward regions, the Forward Multiplicity Detector FMD (3), the Zero Degree Calorimeters ZDCs (11), T0, V0 and a Muon Tracker (10) were located.

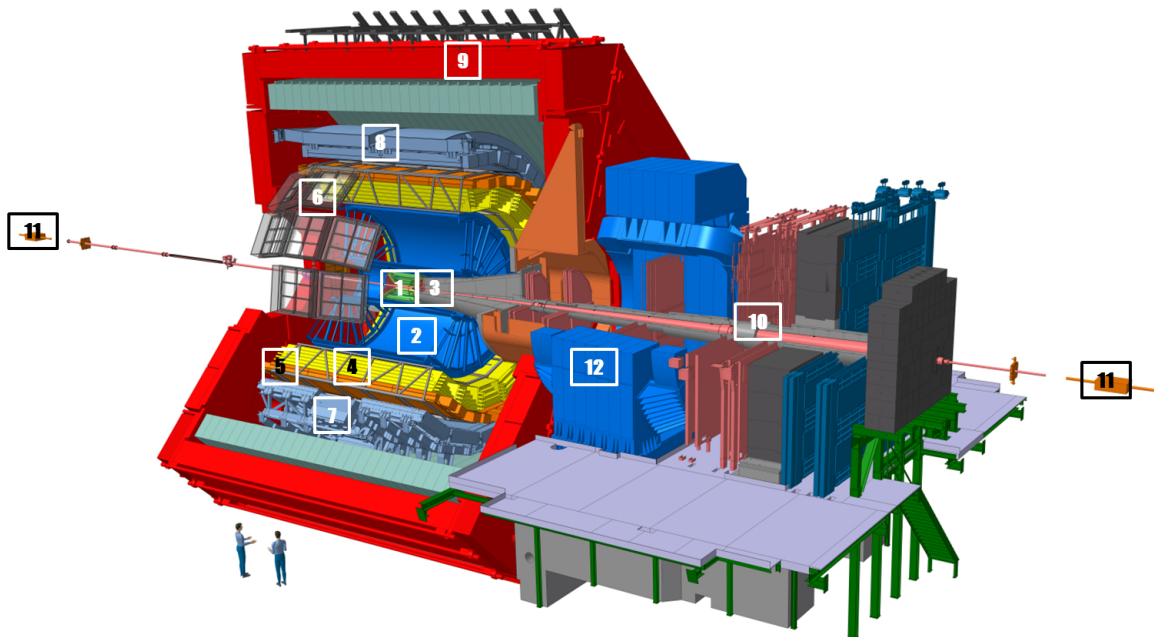


Figure 2.3: The schema of ALICE experiment during Run 2. (1) ITS, (2) TPC, (3) T0, V0, FMD, (4) TRD, (5) TOF, (6) HMPID, (7) PHOS, (8) EMCal, (9) L3 Magnet, (10) Muon tracker, (11) ZDCs, (12) Dipole magnet. Taken from [12] and adjusted.

2.2.1.1 Inner Tracking System

The ITS consisted of three high-resolution silicon tracking detectors with two layers each. The innermost was a pixel detector SPD; the next was a drift detector SDD; the outmost was a strip detector SSD. The scheme is shown in Fig. 2.4. This structure was completely changed during the upgrade.

When a particle went through the SPD, the detector produced two hits. From those hits, the first approximation of a track, called tracklet, was created. The tracklet is

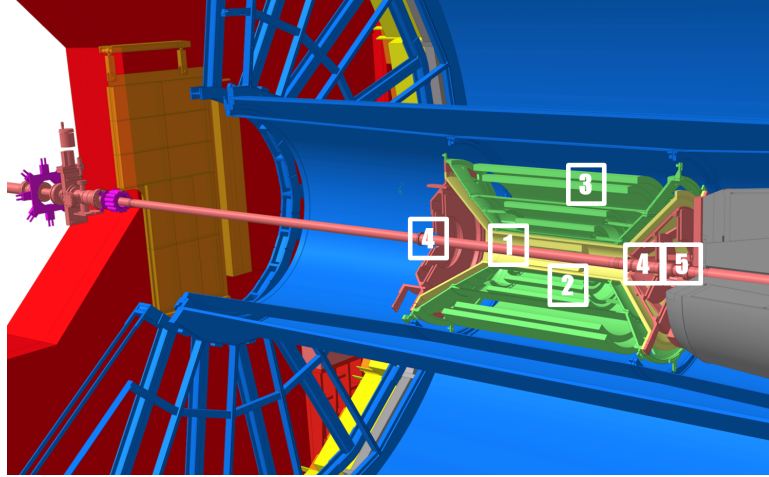


Figure 2.4: The schema of ITS detector during Run 2. (1) SPD, (2) SDD, (3) SSD, (4) FMD, T0, (5) V0. Taken from [12] and adjusted.

a non-curved line, and a set of tracklets is used to make the first approximation of the primary vertex position. When combined with hits from the other two silicon detectors, the ITS was able to determine the primary vertex position with a resolution of $100\ \mu\text{m}$. It was also reconstructing secondary vertices created by hyperon decays. Moreover, it provided the identification of low momentum particles.

The pseudorapidity range of the SPD was $|\eta| < 2$, but for the ITS as a whole, it was only $|\eta| < 1.3$.

2.2.1.2 Time Projection Chamber

The next layer of the central barrel is the TPC. The TPC, being the main tracking detector, was designed to measure the highest multiplicities possible at the LHC energies. It covers a pseudorapidity range of $|\eta| < 0.9$ and the whole circle in the azimuthal angle. The main structure of this detector stayed the same after LS2 and is shown in Fig. 2.5.

The chamber has the shape of a cylinder with two end plates and a central electrode. It is filled with gas, which gets ionized along the path of a passing particle. That results in freeing electrons that drift towards the end plates of the chamber, where their signal gets detected and amplified. The end plates used to be made of multi-wire proportional chambers, but now it uses GEM technology, and it is capable of continuous readout.

2.2.1.3 Time-of-Flight Detector

The TOF detector, with a pseudorapidity range of $|\eta| < 0.9$, identifies particles in the intermediate momentum range and provides a trigger for ultra-peripheral collisions and cosmic ray events. During the LS2 upgrade, the structure of the TOF detector did not change.

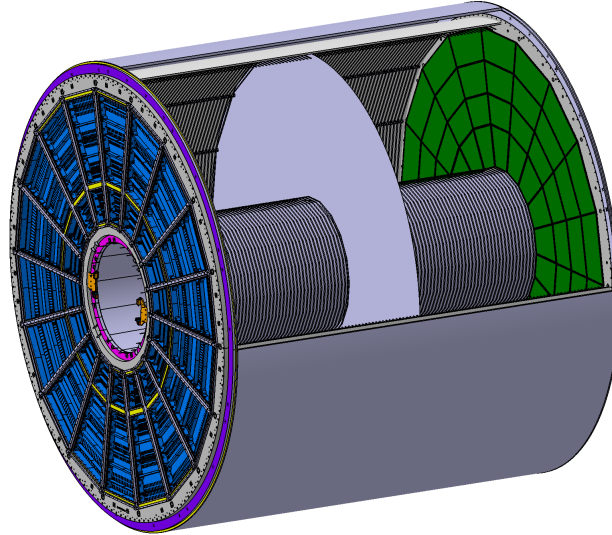


Figure 2.5: The schema of TPC. Taken from [13].

2.2.1.4 The Forward Region Detectors

Information in this subsection is taken from [14].

In the forward and backward regions, the main detectors are the ZDCs, which are supposed to determine the centrality of collisions. These detectors were not changed during the LS2, but the electronics have been upgraded for continuous readout.

Very close to the ITS chamber the T0 detectors were located. They were composed of an array of PMTs with Cherenkov radiators each. T0C and T0A covered the pseudorapidity regions of $-3.3 < \eta < -2.9$ and $4.5 < \eta < 5.0$, respectively. They provided fast timing signals for triggering.

Between the T0s and the ZDCs, the V0 detector, a double-layered ring of plastic scintillator cells, was placed. This detector was, like the T0s, used for triggering. It also helped reject beam-gas events.

To determine the total particle production in proton-proton and lead-lead collisions, Forward Multiplicity Detectors (FMDs) were used, which also measured multiplicity fluctuations. They consisted of more than 50000 silicon strip channels divided into five rings each. The pseudorapidity range coverage was $-3.4 < \eta < -1.7$ and $1.7 < \eta < 5.0$. Combined with the information from ITS, the FMDs provided charged particle multiplicity distributions in the range $-3.4 < \eta < 5.0$.

During the upgrade, the T0, V0 and FMD detectors were replaced by the Fast Interaction Trigger (FIT), which is discussed in the subsection 2.2.2.3.

2.2.2 Upgrade of detectors for the LHC Run 3

As stated before, the ALICE detector was upgraded during the Long Shutdown 2 (LS2) in 2019 and 2020. The plan was to increase the readout rate by two orders

of magnitude to process up to 10^{11} lead-lead collisions per month at a 50 kHz interaction rate. The older interaction rate was 8 kHz and 500 kHz for lead-lead and proton-proton collisions, respectively. The planned measurements for proton-proton collisions will start at an interaction rate of 500 kHz but could go up to 1 MHz. Other planned changes were to add a vertex tracker for forward muons (MFT), to upgrade the ITS and the TPC, and to create the Online-Offline software O², which would replace the old separated online and offline systems and the High Level Trigger (HLT). The new structure is shown in Fig. 2.6.

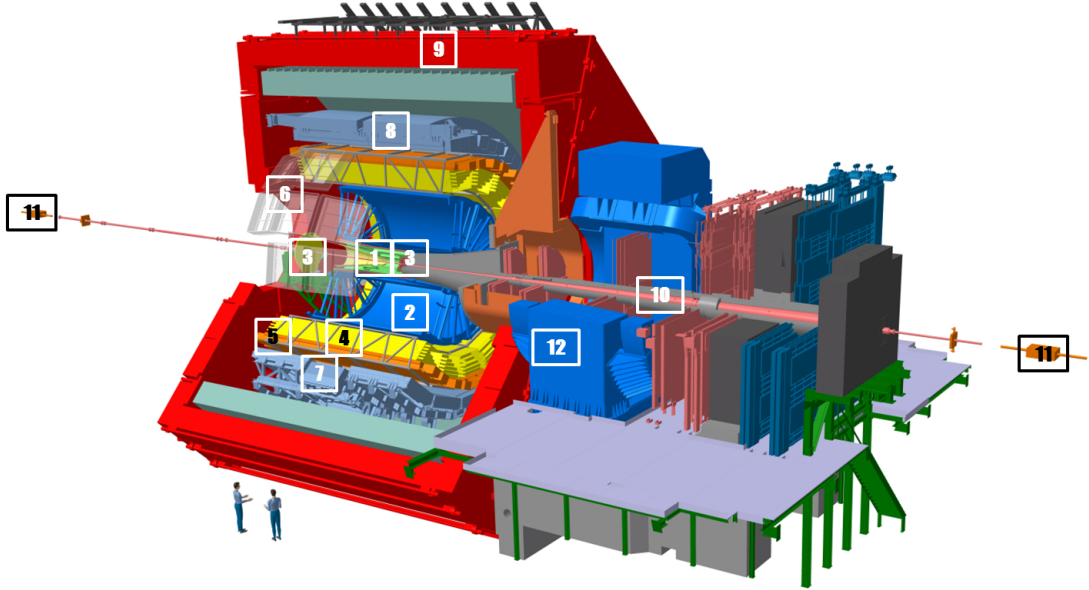


Figure 2.6: The schema of ALICE experiment during Run 3. (1) ITS, (2) TPC, (3) FT0 (left and right), FV0 (left), FDD (left and right), (4) TRD, (5) TOF, (6) HMPID, (7) PHOS, (8) EMCAL, (9) L3 Magnet, (10) Muon tracking chambers, (11) ZDCs, (12) Dipole magnet. Taken from [12] and adjusted.

2.2.2.1 Upgraded Inner Tracking System

Previously, it was mentioned that the whole structure of the ITS was changed during the upgrade. The ITS detector is now composed of three inner layers and four outer layers of pixel detectors. The schema is shown in Fig. 2.7. These changes should improve the track position resolution at the primary vertex by a factor of three and the determination of the distance of the closest approach of the tracks to the main vertex. It also provides new measurements on charm and beauty production by extending the measured range to very low p_T .

The seven layers of this detector should be enough to reconstruct whole tracks based only on the information given by the ITS. The new spatial resolution is about 5 μm .

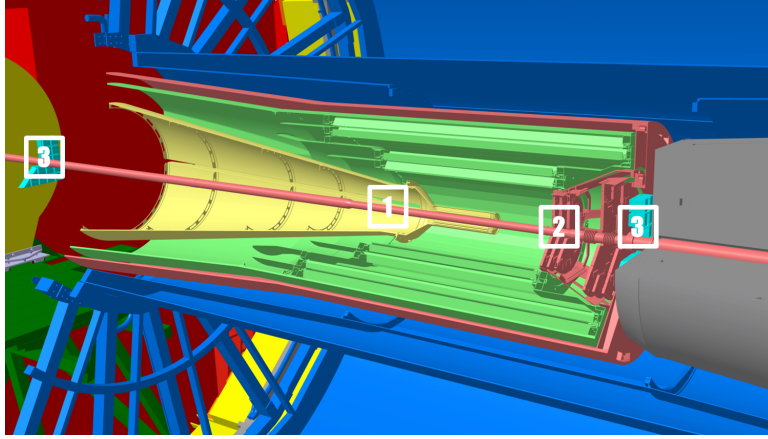


Figure 2.7: The schema of ITS detector during Run 3. (1) ITS, (2) MFT, (3) FT0-A (left), FT0-C (right). Taken from [12] and adjusted.

2.2.2.2 Upgraded Time Projection Chamber

The main upgrade of the TPC is a continuous readout to process data from collisions happening each $20 \mu\text{s}$ and up to 5 overlapping events. To achieve this, the Multi-Wire Proportional Chambers were replaced by Gas Electron Multipliers (GEMs).

2.2.2.3 Fast Interaction Trigger

This section is based on information taken from [15].

With the continuous readout, a very fast triggering system became necessary. The Fast Interaction Trigger (FIT) replaced the previous T0 and V0 detectors with new versions called FT0 and FV0 or sometimes T0+ and V0+. The FIT is complemented by the Forward Diffractive Detector (FDD). The schema of FIT is shown in Fig. 2.8.

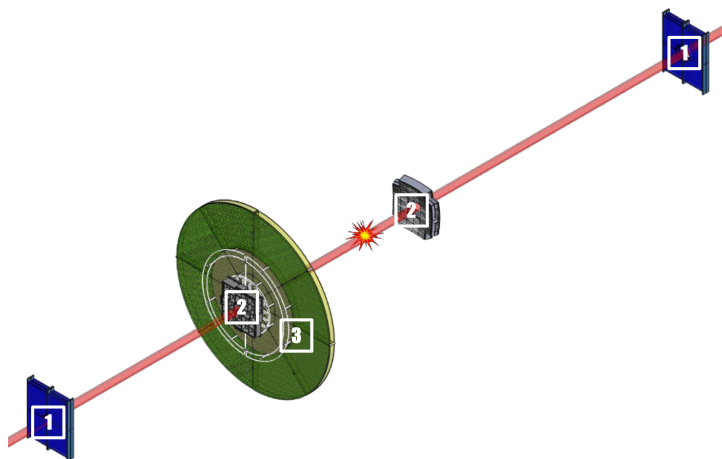


Figure 2.8: The schema of FIT during Run 3. (1) FDDs, (2) FT0, (3) FV0. Taken from [15] and adjusted.

The new FT0 still has a Cherenkov detector array and works as a timing system. It also has an excellent signal-background ratio. Similarly, the new FV0 is still composed of plastic scintillator cells arranged in rings. However, it has an improved trigger efficiency and dynamic range.

The FV0 has only one array located in the positive pseudorapidity section. Unlike that, the FT0 and FDD have an arm in both the positive and negative sections. Therefore, a coincidence trigger can be used to reject beam-gas events. This results in a minimum contribution from background effects in the data.

The FIT detector works as a minimum bias (MB) trigger and multiplicity-based trigger. The triggering system is governed by the Central Trigger Processor (CTP), which collects and processes trigger signals and converts them into formats accepted by the Local Trigger Units (LTUs). Then, the detector signals are sent to Common Readout Units (CRUs), where the data flow from detectors to the O² system is controlled.

Each trigger has its own set of requirements. The MB trigger, used for proton-proton and proton-lead collisions, needs to select only events with collisions, but it needs to select them all. The Multiplicity trigger has to maximize multi-particle detection efficiency. Moreover, the dynamic range has to be bigger than the expected maximum of particles. This all can be achieved either by a very high granularity, which would not meet the timing requirements or by low granularity but with pixels being able to detect the number of particles it has been hit by.

To summarise this subsection, the upgrade of T0 and V0 detectors and the addition of the FDD provides us with a clean trigger and a set of detectors able to measure multiplicity and collision time with high precision.

2.2.2.4 Muon Forward Tracker

Information in this section is based on [16].

The MFT is a silicon tracking detector added to the Muon Spectrometer to improve the identification of secondary vertices and mass resolution. It covers the pseudorapidity range $-3.6 < \eta < -2.5$.

The MFT is based on the same pixel technology as the ITS. It consists of five disks containing half a billion pixels. The readout electronics used for the MFT are the same as those of the new ITS.

Adding this detector gives us a higher spatial resolution of tracks of charged particles and a stronger rejection of background muons created from pion or kaon decays.

2.2.2.5 Online-Offline system

Information in this chapter is taken from [17].

The expectation is that the upgraded LHC will be producing a hundred times more measurable lead-lead central collisions than it was during Run 2. This is partly

because of the higher collision rate and partly because of the elimination of deadtime. ALICE is going to manage this using continuous readout mode. This means that a new analysis software is needed for Run 3. The ALICE collaboration decided to upgrade the previous High Level Trigger (HLT) and, in collaboration with the FAIR experiment at GSI, developed the Online-Offline system called O².

The O² software was designed to compress data and partially reconstruct events to achieve higher efficiency of data storing. As a result, it should be able to process 3 TB of raw data per second and store on average 10 GB per second.

The raw data are firstly reduced in size by the 150 First Level Processors (FLPs) to approximately 500 GB/s. Next, the data divided into so-called "uncompressed time frames" of the size of 10 GB, containing 23 ms of continuous readout data, are compressed and partially reconstructed by Event Processing Nodes (EPNs), creating "compressed time frames" of 2 GB on average. The EPN comprises 250 servers able to do a real-time online reconstruction as described. In addition, while not taking data, EPNs can be used for analysis and processing during the asynchronous offline phase.

The O² software has three major parts: the Transport Layer FairMQ, the O² Data Model and the Data Processing Layer (DPL). The Transport Layer has been developed at GSI, and it covers the communication among devices.

The O² Data Model has been built by the ALICE team, and it covers the description of the messages sent between devices. Each message is composed of a header describing the data origin (detectors or processes) and the type of data contained in the second part, which is a payload. This software is compatible with ROOT and supports multiple data formats and serializations. It has three key features: it is not committed to a specific programming language, it is extensible, and it uses an efficient transport of data between shared and GPU memory.

The last part of the whole Online-Offline system is the Data Processing Layer (DPL). It describes complex computation processes as organized data processors, and it is capable of creating an optimized topology for any process. The whole complexity is hidden from the end-user. He or she simply chooses an environment and runs a single executable called the DPL driver, which maps the dataflow to the optimized topology and efficiently connects the chosen set of processes. An example of a user interface is shown in Fig. 2.9.

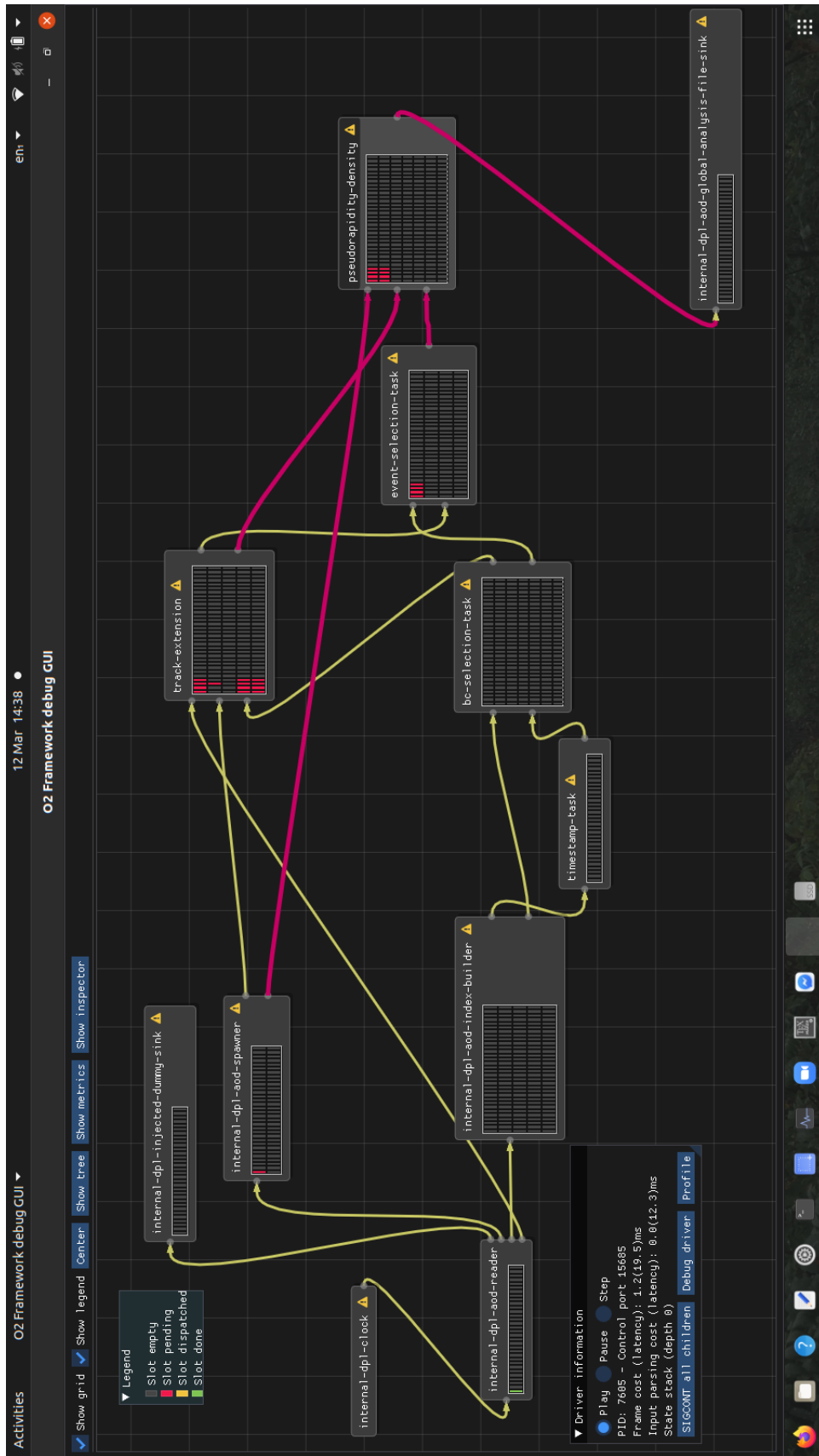


Figure 2.9: An example of user interface of O².

Chapter 3

Previous related work

Measurements of proton-proton collisions at the LHC started in 2009. Before that, the Super Proton Synchrotron at CERN operated as a proton-antiproton collider since 1981 [18].

The collision analysis process is long and complex. The first reconstructed observable is usually the multiplicity. To get the multiplicity, a physicist needs only the number of tracks. There is no need to know the momenta or charges of particles or to identify them.

The multiplicity measurements in ALICE during Run 1 and Run 2 were obtained from the number of tracklets recorded with the two SPD layers of the ITS. Now, during Run 3, the ITS should be able to reconstruct the whole track; therefore, the new measurement of the multiplicity should be more precise.

When the multiplicity is differentiated with respect to pseudorapidity, it is equal to a variable called the pseudorapidity density, which is another obtained observable. The total multiplicity in a given pseudorapidity range is then obtained by integrating the pseudorapidity density over said range.

Both multiplicity and pseudorapidity density are observables mostly used to characterize events, but their measurements can also be used, for instance, for testing the presence of quantum entanglement.

This chapter starts with the summary of the first measurements of proton-proton collisions done with ALICE [1] in Section 3.1, nextly, the measurements done with ALICE during the Run 2 [2] are described in Section 3.2, and lastly, the use of measured multiplicity data in testing the presence of quantum entanglement is explained in Section 3.3.

3.1 Measurements of pp collisions at $\sqrt{s} = 0.9$ TeV

In November of 2009, there was a test run of the newly built LHC. The counter-rotating proton bunches had the injection energy of 450 GeV and low intensity with only one bunch per beam. Even though no systematic attempt to optimize the crossings was done, 284 collisions were recorded by the ALICE detector and analysed using both online and offline software. The results were published in 2010 [1].

Two classes of events were analysed: the INEL class containing all inelastic events and the NSD class containing non-diffractive, central-diffractive and double-diffractive events but rejecting all single-diffractive events. For the analysis itself, only data from the SPD part of the ITS were used. Data from the SDD, SSD and the V0 detectors were used for the cross-checks and background removal. Using both layers of the SPD, the events were analysed in the pseudorapidity region $|\eta| < 1.6$.

The vertex reconstruction efficiency was obtained using Monte Carlo simulations and for the range $|z| < 10$ cm of the z axis, it was 84% and 92% for the INEL and NSD classes, respectively. With a wider range of the z coordinate of the vertex, the efficiency decreases, so the analysis stayed in the ± 10 cm limit. The vertex position distribution along the z axis is shown in Fig. 3.1.

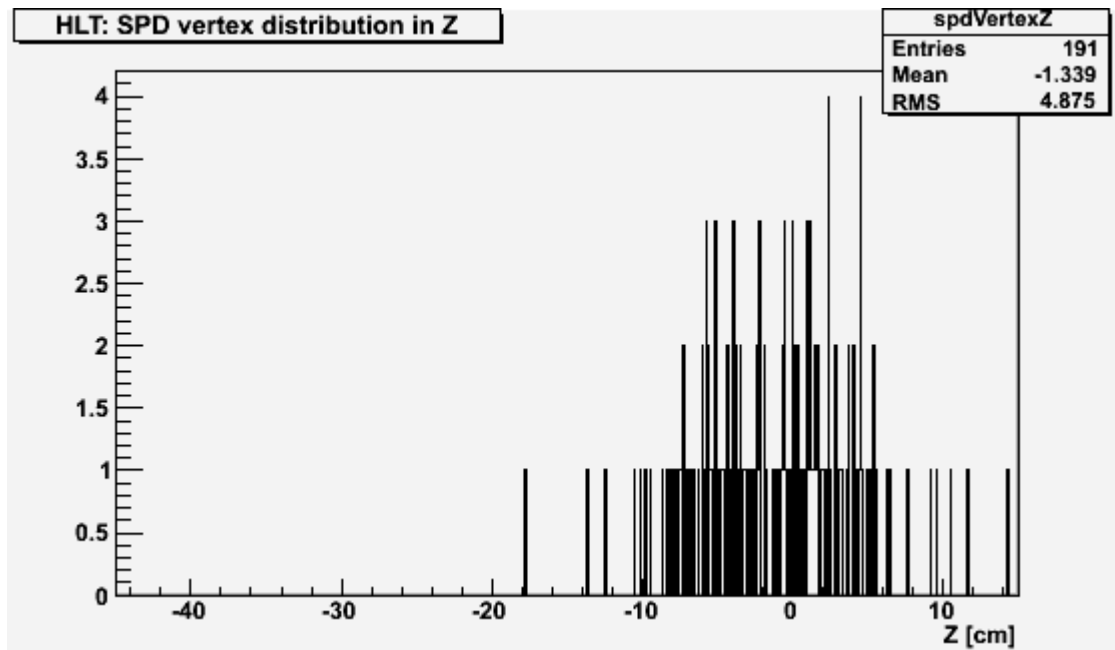


Figure 3.1: Vertex position distribution along the z axis. Taken from [1].

Corrections for the trigger inefficiency, the detector and reconstruction inefficiencies and the contamination by weak decays and secondary interactions were calculated using GEANT 3 simulations. The final systematic uncertainty of the pseudorapidity density was less than $\pm 7.2\%$ for the INEL events and $\pm 7.1\%$ for the NSD events.

The measured pseudorapidity density in the pseudorapidity range $|\eta| < 0.5$ was $dN_{\text{ch}}/d\eta = 3.10 \pm 0.13$ (stat.) ± 0.22 (syst.) for the INEL class and $dN_{\text{ch}}/d\eta =$

3.51 ± 0.15 (stat.) ± 0.25 (syst.) for the NSD class. This result is consistent with previous measurements of proton-antiproton collisions. The dependence of pseudorapidity density on pseudorapidity for proton-proton and proton-antiproton collisions is shown in Fig. 3.2 for both the INEL and NSD classes.

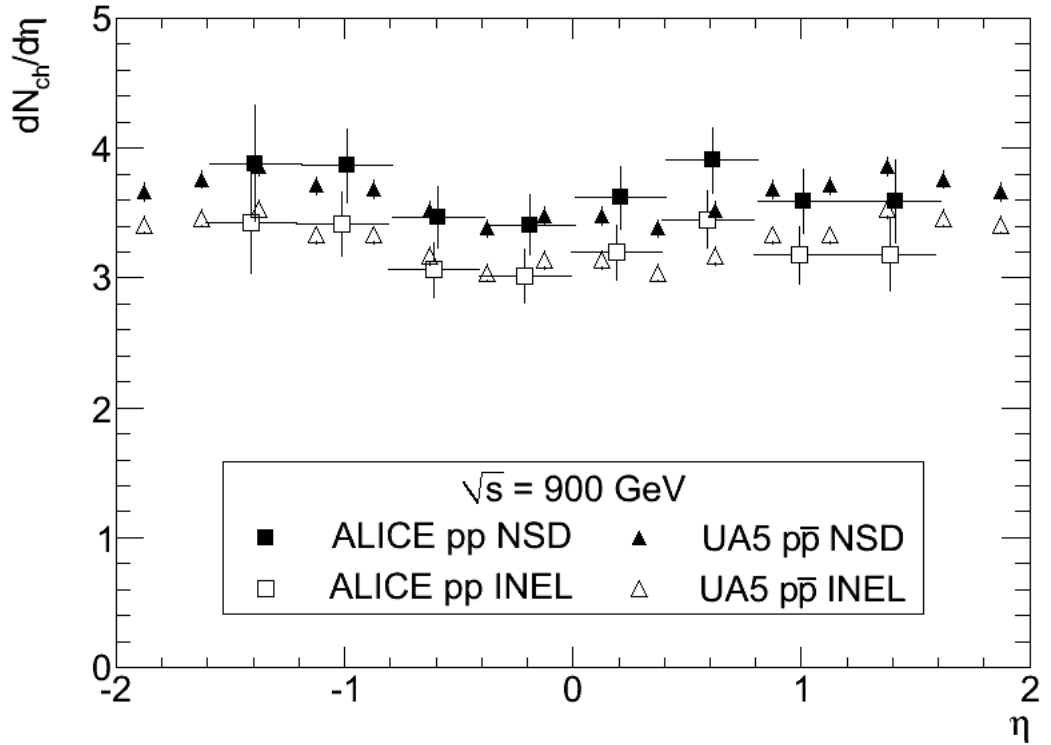


Figure 3.2: Pseudorapidity dependence of pseudorapidity density for proton-proton and proton-antiproton collisions and for the INEL and NSD classes. Taken from [1].

3.2 Measurements of pp collisions at $\sqrt{s} = 0.9$ to 8 TeV

During the LHC Run 2, the ALICE detector was used to study multiplicity distributions and pseudorapidity densities of primary charged particles in proton-proton collisions. A detailed study by the ALICE Collaboration was published in January of 2017 [2].

Measurements were carried out for three event classes: inelastic events (INEL), non-single diffractive events (NSD) and events with at least one primary charged particle in the pseudorapidity range $|\eta| < 1$ (INEL >0). Multiplicity distributions and pseudorapidity densities of primary charged particles were studied for collisions at $\sqrt{s} = 0.9, 2.76, 7$ and 8 TeV in three pseudorapidity intervals: $|\eta| < 0.5, 1.0$ and 1.5.

The findings of this study provide data for comparing proton-proton collisions and gold-gold central collisions with similar energy densities but volumes of orders of magnitude different. They may also contribute to the creation of advanced models of lead-lead collisions. Furthermore, a comparison of the collected real data to the hadron collision models showed that contemporary collision generators are inadequate and insufficient. Both soft processes and hard scatterings were studied.

The principal result of this study is a smooth evolution of multiplicity distributions and pseudorapidity densities of charged particles at center-of-mass energies from $\sqrt{s} = 0.9$ TeV to $\sqrt{s} = 8$ TeV.

3.2.1 Track counting algorithms

One of the upgrades for this study was improved track counting algorithms. Three different algorithms were used: Tracklet, ITS+ and ITSTPC+. The first one used only data from the SPD in the range of pseudorapidity $|\eta| < 2$, the second one combined that with the tracks from ITS in the range $|\eta| < 1.3$ and the last one used SPD tracklets and ITS tracks in their respective ranges plus it adds the TPC tracks in the range $|\eta| < 0.9$.

Figure 3.3 shows the dependence of measured multiplicity on generated multiplicity. The Tracklet algorithm is the least accurate, the ITSTPC+ is the most accurate, and the accuracy for all three algorithms falls with wider pseudorapidity ranges.

3.2.2 Pseudorapidity densities

The distributions of pseudorapidity density $dN_{\text{ch}}/d\eta$ were one of the studied quantities. First, the raw data needed to be corrected for detector and trigger acceptance and appearances of strange particles. Second, the corrected data underwent event class normalisation. Finally, the processed data were compared to previous studies, data acquired from Monte Carlo simulations and measurements of lead-lead

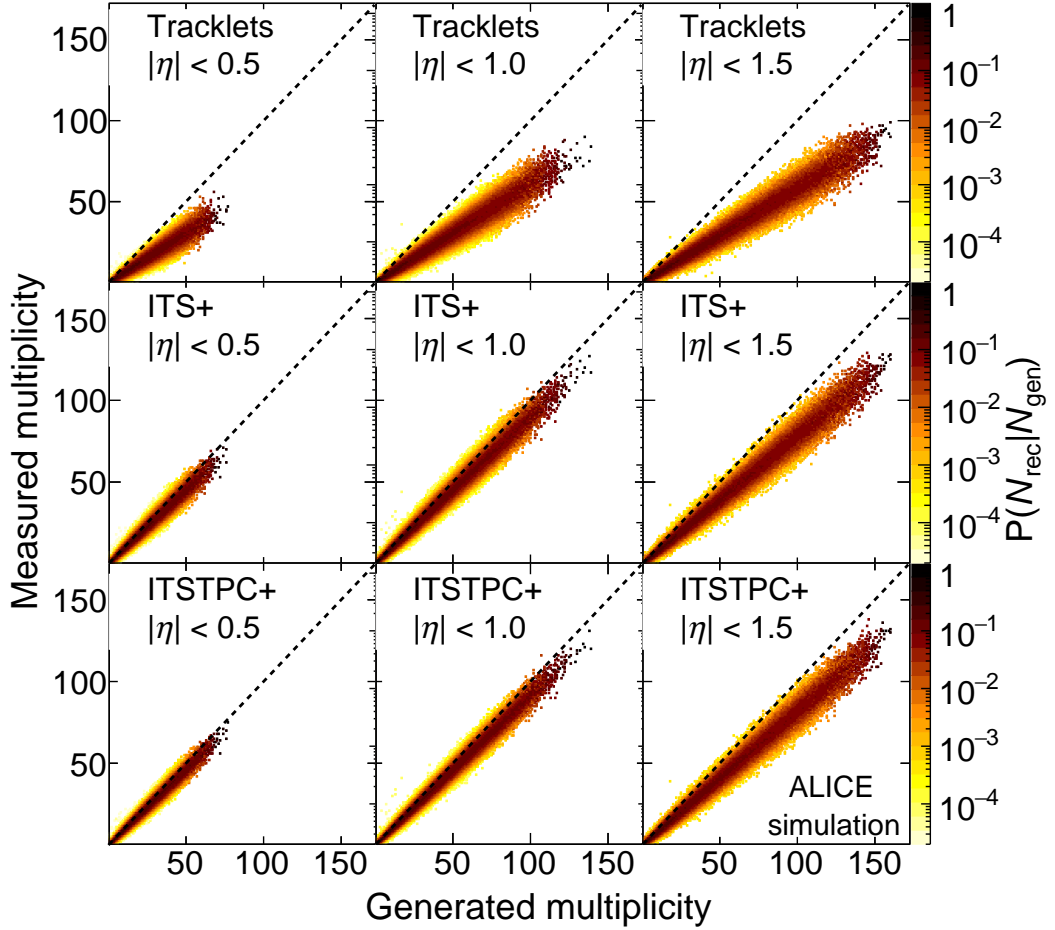


Figure 3.3: Graphical representation of the detector response matrices obtained with PYTHIA 6 CSC combined with a simulation of the ALICE detector at $\sqrt{s} = 7$ TeV. Taken from [2].

collisions.

3.2.2.1 Detector and trigger corrections

The corrections for detector and trigger acceptance and efficiency were done in three stages. Firstly, there was a correction for differences between measured tracks and the real charged primary particles occurrence. Next, the bias from the number of tracks and events for the vertex reconstruction had to be corrected. And lastly, corrections for bias from triggers MB_{OR} and MB_{AND} needed to be done at both track and event levels. The final pseudorapidity density distribution $dN_{\text{ch}}/d\eta$ is the processed data averaged over all events for each bin.

3.2.2.2 Strangeness corrections

As the primary charged particles at ALICE do not include particles from weak decays, all daughters from strange particles need to be excluded. That is done

automatically, but some of those particles make the cut by mistake. Therefore, there has to be a correction for those that passed the track selection. What was found in this study is that the contamination from the decays of the strange particles is slightly dependent on pseudorapidity.

3.2.2.3 Event class normalisation

As stated before, the corrected data still needs to be normalised for each event class. The normalisation involves the corrections for trigger bias on both track and event levels.

For the non-single diffractive (NSD) events, one more correction is needed to reject the few single diffractive (SD) events remaining and to include some double diffractive (DD) events that did not make the cut before.

The INEL event class, which includes all the inelastic events, sometimes lacks some SD and DD events that need to be included.

And lastly, the event class of inelastic events with at least one primary charged particle in the pseudorapidity interval $|\eta| < 1$ (INEL>0) minimizes the diffractive events. Therefore, it has to be corrected for the SD and DD events that passed the track selection.

3.2.2.4 Experimental results

The pseudorapidity density has been measured for proton-proton collisions several times before. Moreover, multiple Monte Carlo generators offer predictions for this observable. Therefore, there is a lot of data with which the new measurements can be compared.

The systematic uncertainties show no pseudorapidity variation in the whole studied pseudorapidity range $|\eta| < 2$, and the statistical uncertainties are negligible compared to systematical ones.

As in the common range of pseudorapidity $|\eta| < 0.9$, all three used track-counting algorithms give similar precision of 1% and consistent results; the tracklet algorithm alone was used in the pseudorapidity density $dN_{\text{ch}}/d\eta$ versus pseudorapidity η correlation study, to achieve the largest possible η range. The main difference between the track counting algorithms is that ITS+ and ITSTPC+ need a detector calibration for the TPC and SDD, whereas the SPD does not.

Results for the center-of-mass energy $\sqrt{s} = 0.9$ TeV are shown in Fig. 3.4. For the INEL events, the newly acquired data are slightly lower than previous measurements. This can be explained by some of the improvements made: better tuning of the Monte Carlo generators was used for diffraction corrections, which has an impact on the sensitivity to single-diffractive events. Also, the strangeness contamination removal system was improved, which can significantly lower the number of suitable charged particles. And the pseudorapidity dependence of the tracklet algorithm was also improved.

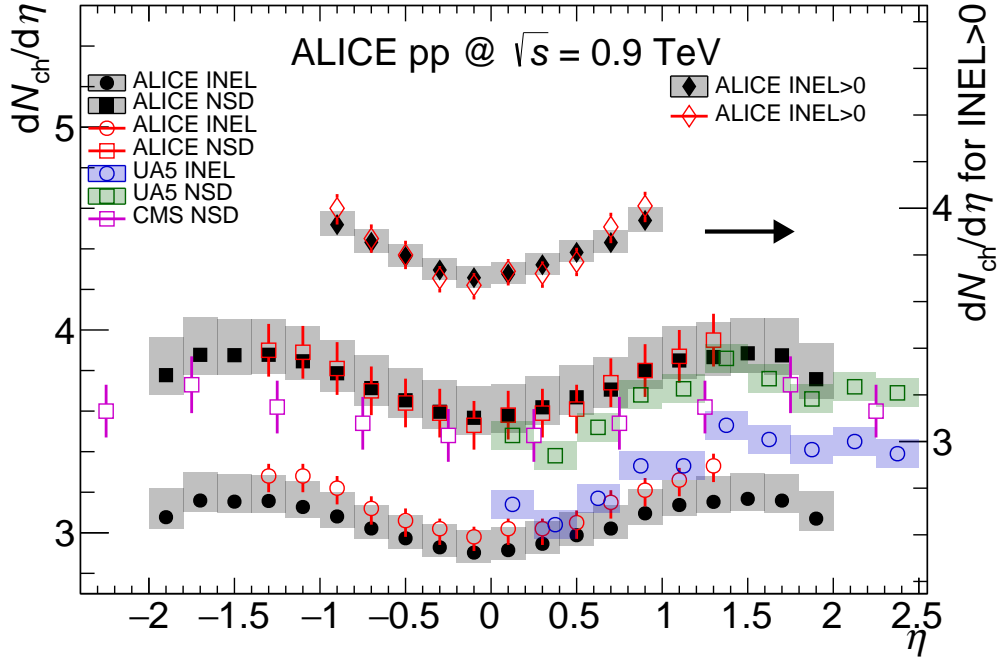


Figure 3.4: Newly and previously measured pseudorapidity density versus pseudorapidity at the center-of-mass energy $\sqrt{s} = 0.9$ TeV. Taken from [2].

For the center-of-mass energy $\sqrt{s} = 2.76$ TeV the results are in Fig. 3.5 and they are consistent with previous measurements at $\sqrt{s} = 2.36$ TeV.

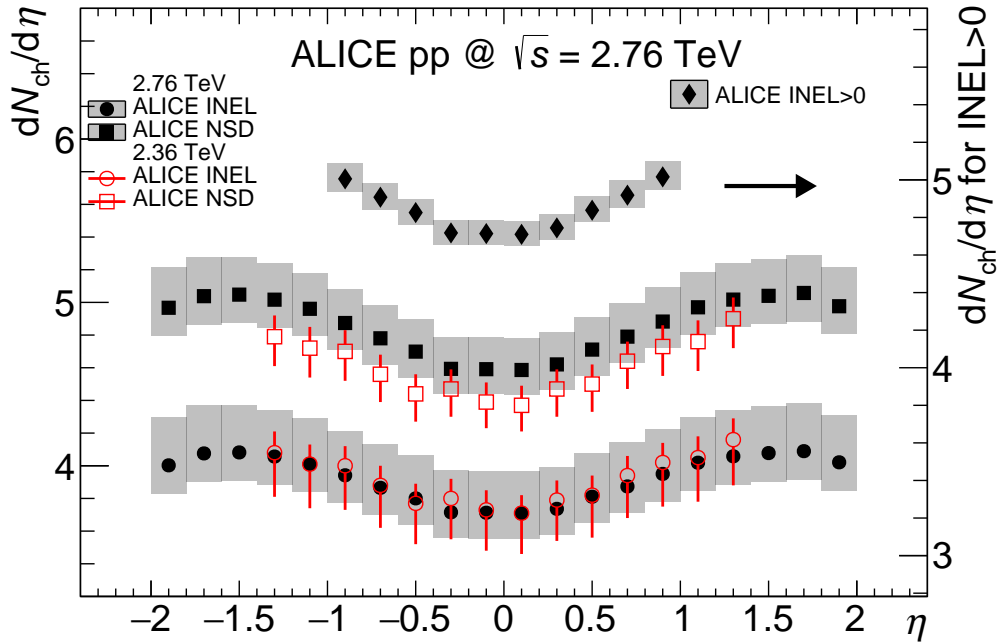


Figure 3.5: Newly and previously measured pseudorapidity density versus pseudorapidity at the center-of-mass energies $\sqrt{s} = 2.76$ TeV and $\sqrt{s} = 2.36$ TeV, respectively. Taken from [2].

Measurements of pseudorapidity density at the energy $\sqrt{s} = 7$ TeV are in agreement with previous CMS data for NSD events and previous ALICE data for INEL>0.

Results and previous measurements done at this energy are in Fig. 3.6.

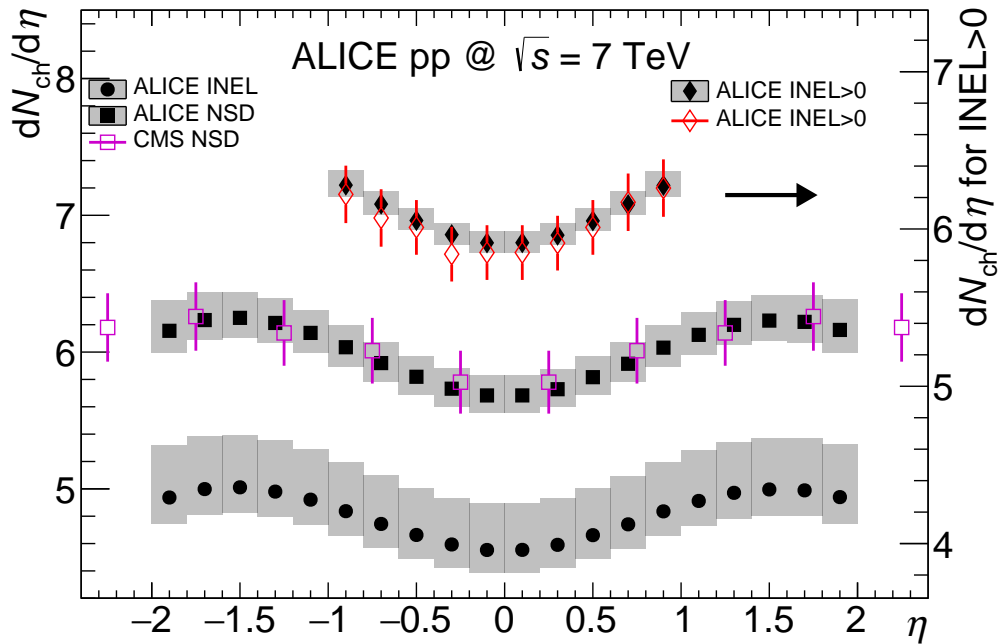


Figure 3.6: Newly and previously measured pseudorapidity density versus pseudorapidity at the center-of-mass energy $\sqrt{s} = 7$ TeV. Taken from [2].

The energy of $\sqrt{s} = 8$ TeV was studied for the first time ever. It has a 3% increase in pseudorapidity density compared to $\sqrt{s} = 7$ TeV, which is in good agreement with extrapolation. The results are shown in Fig. 3.7.

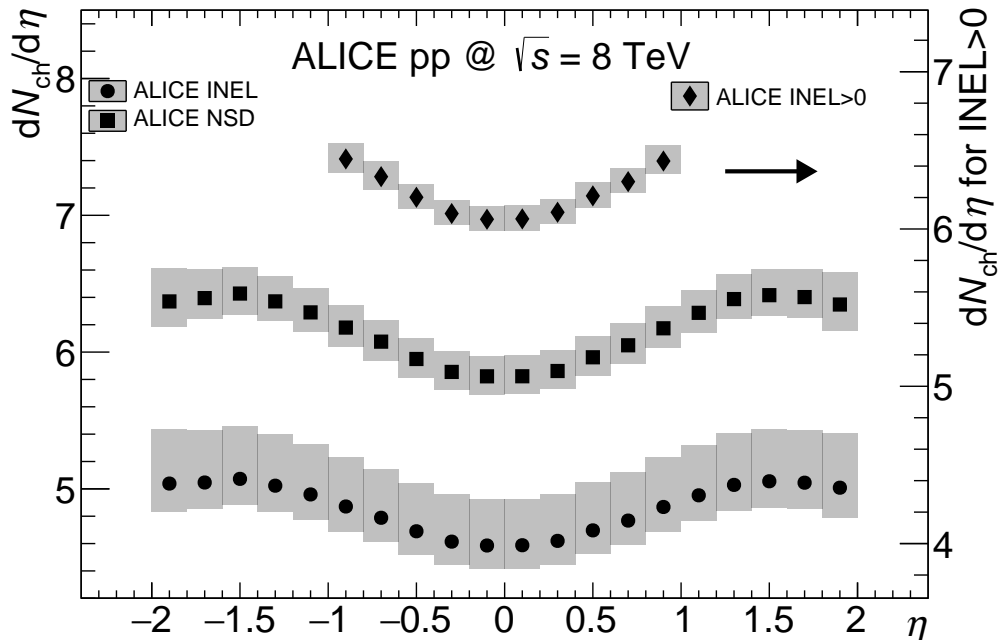


Figure 3.7: Newly measured pseudorapidity density versus pseudorapidity at the center-of-mass energy $\sqrt{s} = 8$ TeV. Taken from [2].

When comparing the shape of the pseudorapidity density distributions for the studied center-of-mass energies, there are no significant discrepancies. Furthermore, there is a visible smooth evolution with increasing energy. This can be seen in Fig. 3.8.

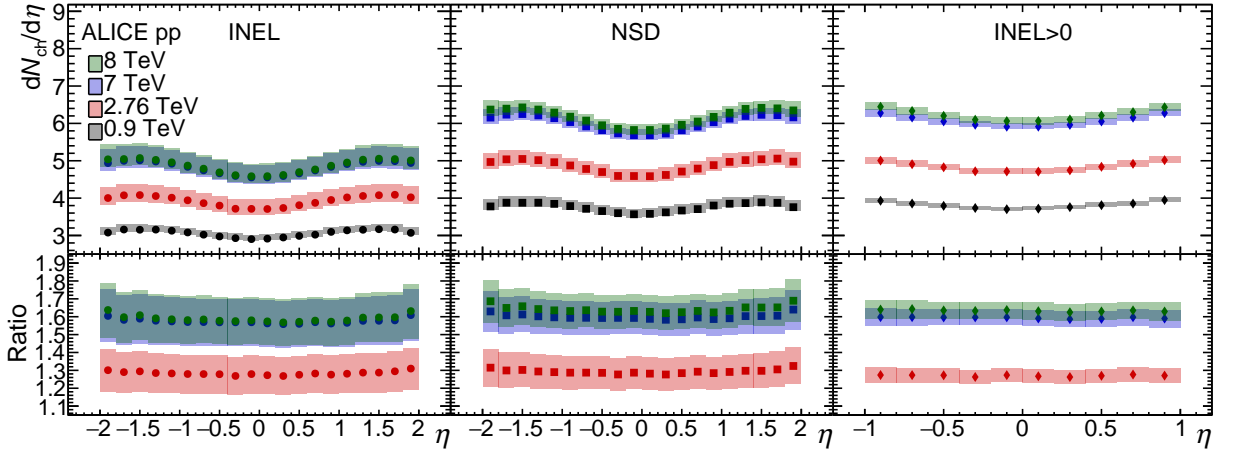


Figure 3.8: Newly measured pseudorapidity density versus pseudorapidity at the center-of-mass energies $\sqrt{s} = 0.9, 2.76, 7,$ and 8 TeV. Taken from [2].

Comparing the measured data with Monte Carlo simulations, it is obvious from Fig. 3.9 that none of the generators are able to describe all the data. Specifically, regarding PYTHIA 8, the generated pseudorapidity density corresponds with the measured data at $\sqrt{s} = 0.9$ TeV, however, at $\sqrt{s} = 7$ TeV it overestimates them. Monte Carlo generators PYTHIA 8 4C, PYTHIA 6 Perugia2011 and EPOS LHC were all tuned using primary LHC data.

Another studied quantity was the energy dependence of the pseudorapidity density at $|\eta| = 0$. The standard formula to calculate this is:

$$\left. \frac{dN_{\text{ch}}}{d\eta} \right|_{\eta=0} = \int_{-0.5}^{0.5} \frac{dN_{\text{ch}}}{d\eta} d\eta. \quad (3.1)$$

This quantity provides information about the basic properties of proton-proton collisions and is related to the average energy density of the event. It gives us a reference to compare with heavy-ion collisions. The achieved results are shown in Fig. 3.10. The relative precision of $dN_{\text{ch}}/d\eta$ at $|\eta| = 0$ for center-of-mass energy $\sqrt{s} = 7$ TeV is for INEL events 5.5%, for NSD events 2.6% and for INEL>0 1.3%.

The energy dependence of the pseudorapidity density can be parametrized at midrapidity as a power law $dN_{\text{ch}}/d\eta \sim s^\delta$. For the pseudorapidity densities calculated at $|\eta| = 0$ the power law parametrization was used and it gave us the following results: for INEL events $\delta = 0.102 \pm 0.003$, for NSD events $\delta = 0.114 \pm 0.003$ and for INEL>0 $\delta = 0.114 \pm 0.001$. After comparison with $\delta \approx 0.15$ for lead-lead collisions, it is obvious that the particle pseudorapidity density does increase faster with energy for lead-lead collisions than for proton-proton collisions.

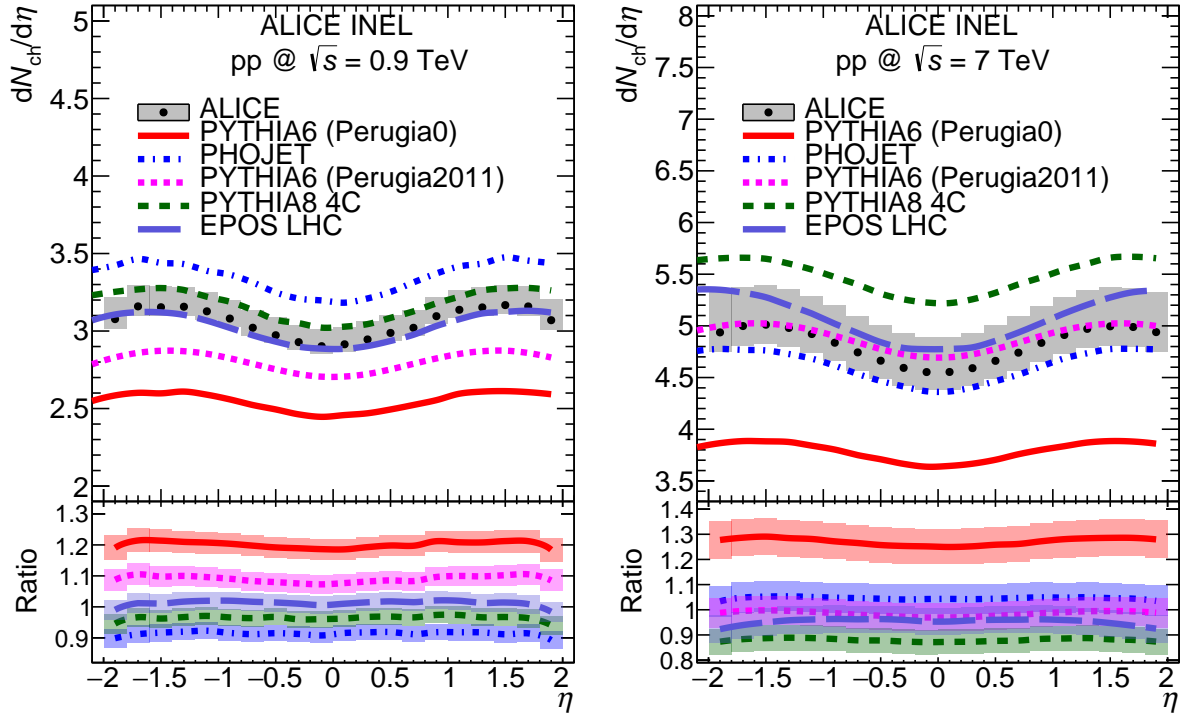


Figure 3.9: Newly measured and simulated pseudorapidity density versus pseudo-rapidity at the center-of-mass energy $\sqrt{s} = 0.9$ TeV (left) and $\sqrt{s} = 7$ TeV (right). Taken from [2].

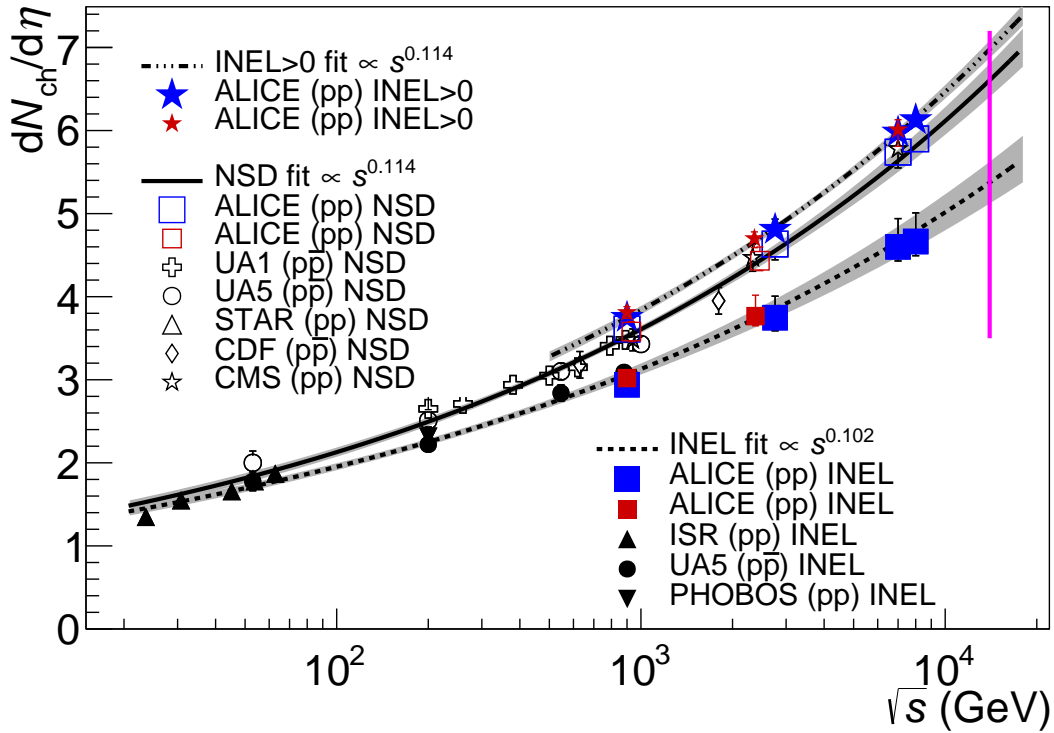


Figure 3.10: Results of the energy dependence of the pseudorapidity density. Taken from [2].

As the first data at a center-of-mass energy $\sqrt{s} = 13$ TeV were acquired before the study was published, an extrapolation of $dN_{\text{ch}}/d\eta$ at $|\eta| = 0$ was created to compare it with the new data. The extrapolation was done with a precision of 4.6%, 3.0%, and 1.3% for INEL, NSD and INEL >0 events, respectively, and is in a good agreement with the new data.

3.2.3 Multiplicity distributions

Other studied quantities were multiplicity distributions $P(N)$. Again the raw data first needed to be processed before they could be used for comparison or description. The process which the raw data underwent is called unfolding.

3.2.3.1 Unfolding

As every man-made detector is imperfect, the data it produces is not true. Measurements in this study are all done discretely, so the relation between the measured data y and the reality x is

$$y_i = R_{ij}x_j, \quad (3.2)$$

where R_{ij} is a so-called response function, in this case, represented by a matrix.

While using detectors with good enough resolution, higher than the binning granularity, the response matrix becomes diagonalizable. A diagonal matrix is easy to inverse, which is needed for correcting the measured data using the relation:

$$x_j = R_{ji}^{-1}y_i. \quad (3.3)$$

However, that is not usually the case, and it is not the case here too. ALICE detectors have a resolution lower than the granularity of bins, which means that sometimes the detectors measure an event in the wrong bin. This leads to a non-diagonal response matrix that is very difficult to inverse.

To acquire corrected data, an unfolding method needs to be applied. This method creates an approximation of the response matrix using some bias. In this case, Monte Carlo simulations were used as the required bias for the corrections for detector acceptance and efficiency.

The efficiency uncertainties are relevant only at multiplicity levels lower than $N = 8$. Apart from the pseudorapidity density, which has uncertainties independent of pseudorapidity, the multiplicity distribution has a variation of total systematic uncertainties dependent on multiplicity.

3.2.3.2 Scaling and fit functions

The Koba-Nielsen-Olesen (KNO) scaling was used to describe the multiplicity distribution. It expresses the probability function $P(n)$ as a function of the mean number of particles $\langle n \rangle$. At sufficiently high energy, this distribution should have the following asymptotic structure:

$$P(n) = \frac{1}{\langle n \rangle} \Psi \left(\frac{n}{\langle n \rangle} \right), \quad (3.4)$$

where Ψ is expected to be an energy invariant shape.

The KNO scaling was already proved to be violated for INEL events at energies $\sqrt{s} \approx 50$ GeV and higher, but for NSD events it held up to $\sqrt{s} \approx 7$ TeV.

This study showed that the KNO scaling for NSD events is also violated. Moreover, it showed that the violation appears already at energies $\sqrt{s} = 2.76$ TeV and that it increases with increasing energy and the size of the pseudorapidity ranges, all of which can be seen in Fig. 3.11.

The measured multiplicity distributions were fitted using single and double negative binomial distributions (NBD). The double NBD is simply a weighted sum of two independent single NBDs. Generally, a double NBD is a better fit for all the measured data, as it accounts for both soft and hard processes. Single NBD can be used to describe only NSD events at $\sqrt{s} = 0.9$ TeV with low multiplicity, Fig. 3.12. The discrepancy between single NBD and data gets larger with higher energy for all three event classes: NSD, INEL and INEL >0 , which can be seen in Fig. 3.12, Fig. 3.13 and Fig. 3.14, respectively.

From those graphs, it is also explicit that the probability of finding a large multiplicity event at a fixed large multiplicity, increases with energy. For NSD events the maximum multiplicity grows from approximately 70 for $\sqrt{s} = 0.9$ TeV to 140 for $\sqrt{s} = 8$ TeV. The same can be said about INEL events. And for INEL >0 events it grows from 60 for $\sqrt{s} = 0.9$ TeV to 110 for $\sqrt{s} = 8$ TeV.

3.2.3.3 Comparison to previous studies

Compared to previous measurements, this study provides data using improved tracking and track counting algorithms and compares them with data acquired from advanced generators. Furthermore, it analyses events in expanded pseudorapidity ranges. At energies $\sqrt{s} = 0.9$ and 7 TeV the measurements provide better statistical precision by a factor of 2 compared to previous ones and at energies $\sqrt{s} = 2.76$ and 8 TeV it gives us the first results ever.

Comparison to data previously acquired by ALICE and CMS is shown in Fig. 3.15 and Fig. 3.16. It can be seen that all the results are consistent and that this study provides a higher precision than those before. However, none of the results can be compared to data from ATLAS or LHCb as they use different p_T and $|\eta|$ ranges.

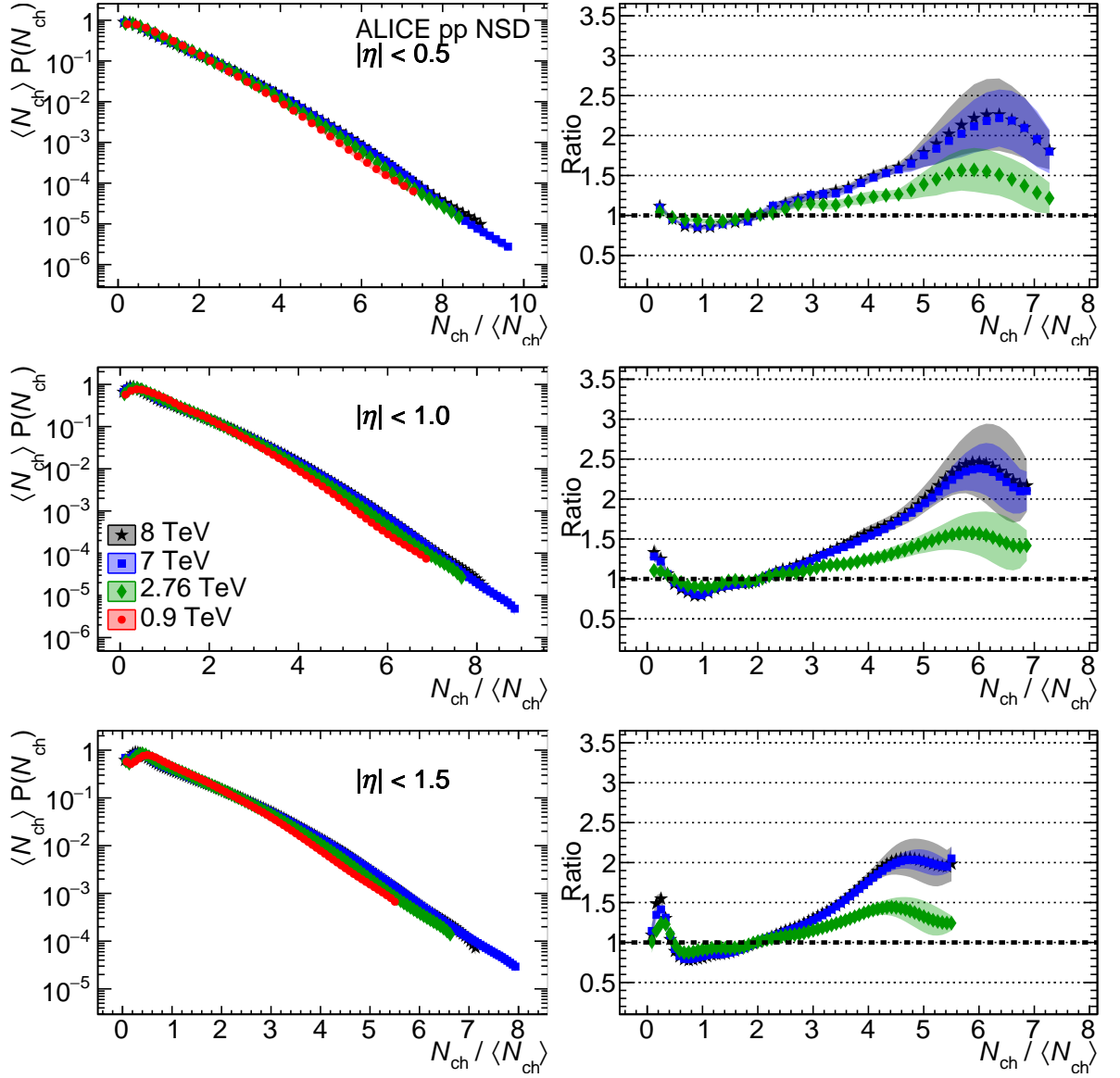


Figure 3.11: KNO scaling of NSD events at energies $\sqrt{s} = 0.9, 2.76, 7,$ and 8 TeV in pseudorapidity intervals $|\eta| < 0.5, 1.0,$ and 1.5 measured by ALICE. Taken from [2].

3.2.3.4 Comparison to models

As mentioned before, current generators fail to describe the real data accurately. Moreover, the disagreement grows with higher multiplicities, as shown in Fig. 3.17. Unsurprisingly, the best fit is provided by the generators adjusted using the first LHC data.

Specifically, regarding PYTHIA 8, multiplicity distribution has a problem at high multiplicities. At $\sqrt{s} = 0.9$ TeV PYTHIA 8 4C underestimates the data above $N_{\text{ch}} \approx 25$ and at $\sqrt{s} = 7$ TeV above $N_{\text{ch}} \approx 60$.

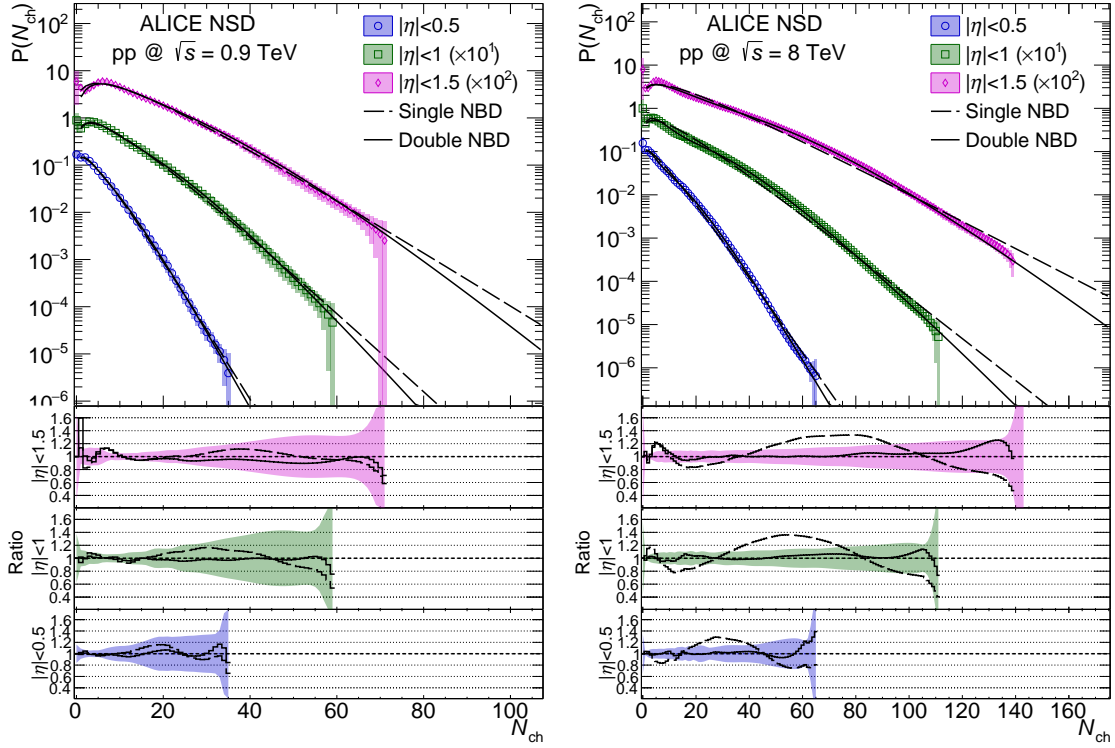


Figure 3.12: NSD events at energies $\sqrt{s} = 0.9$ and 8 TeV in pseudorapidity intervals $|\eta| < 0.5$, 1.0, and 1.5 measured by ALICE, fitted with single and double NBD. Taken from [2].

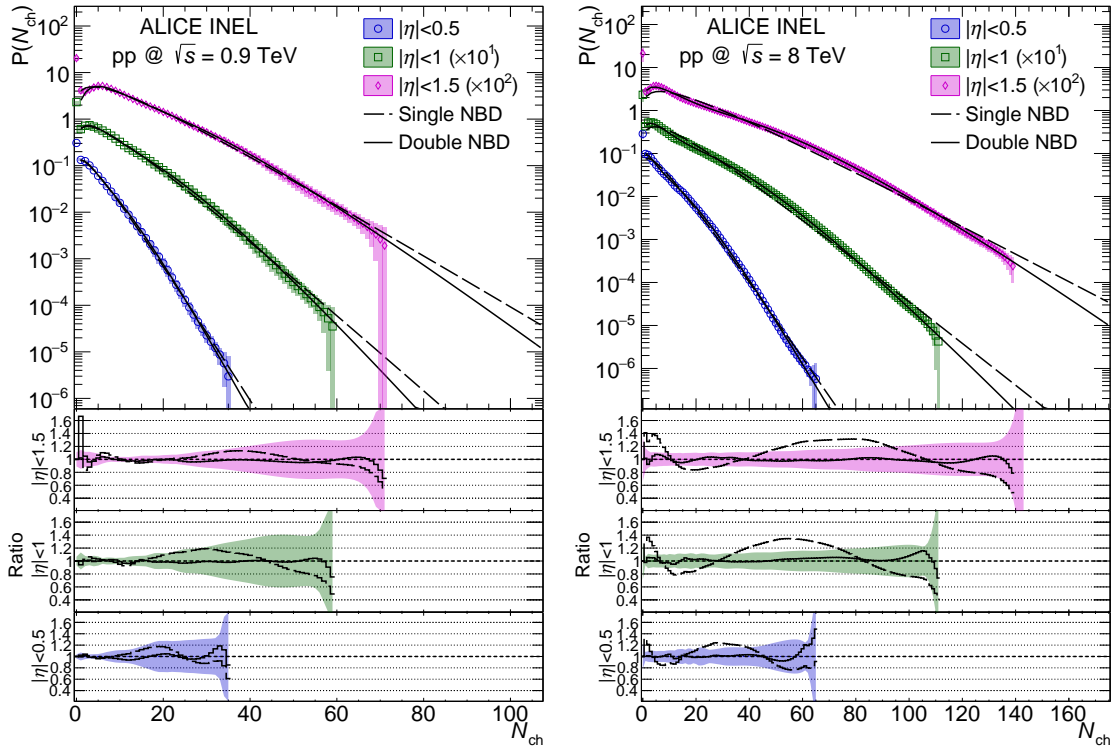


Figure 3.13: INEL events at energies $\sqrt{s} = 0.9$ and 8 TeV in pseudorapidity intervals $|\eta| < 0.5$, 1.0, and 1.5 measured by ALICE, fitted with single and double NBD. Taken from [2].

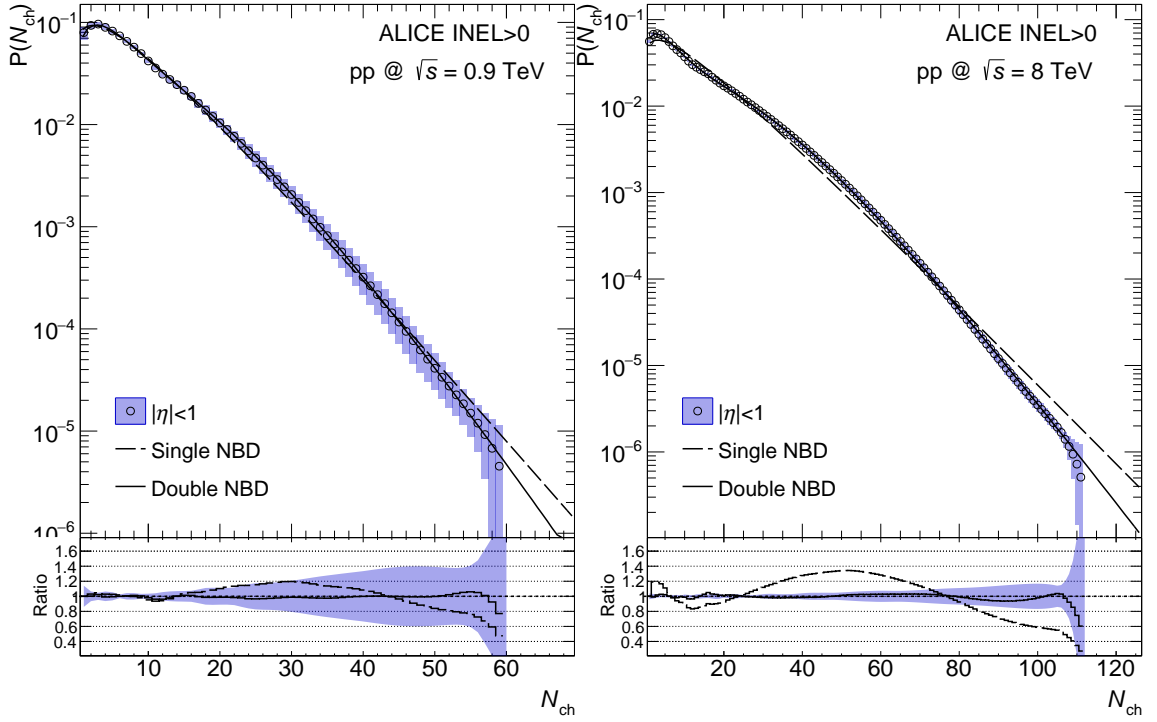


Figure 3.14: INEL>0 events at energies $\sqrt{s} = 0.9$ and 8 TeV in pseudorapidity interval $|\eta| < 1.0$ measured by ALICE, fitted with single and double NBD. Taken from [2].

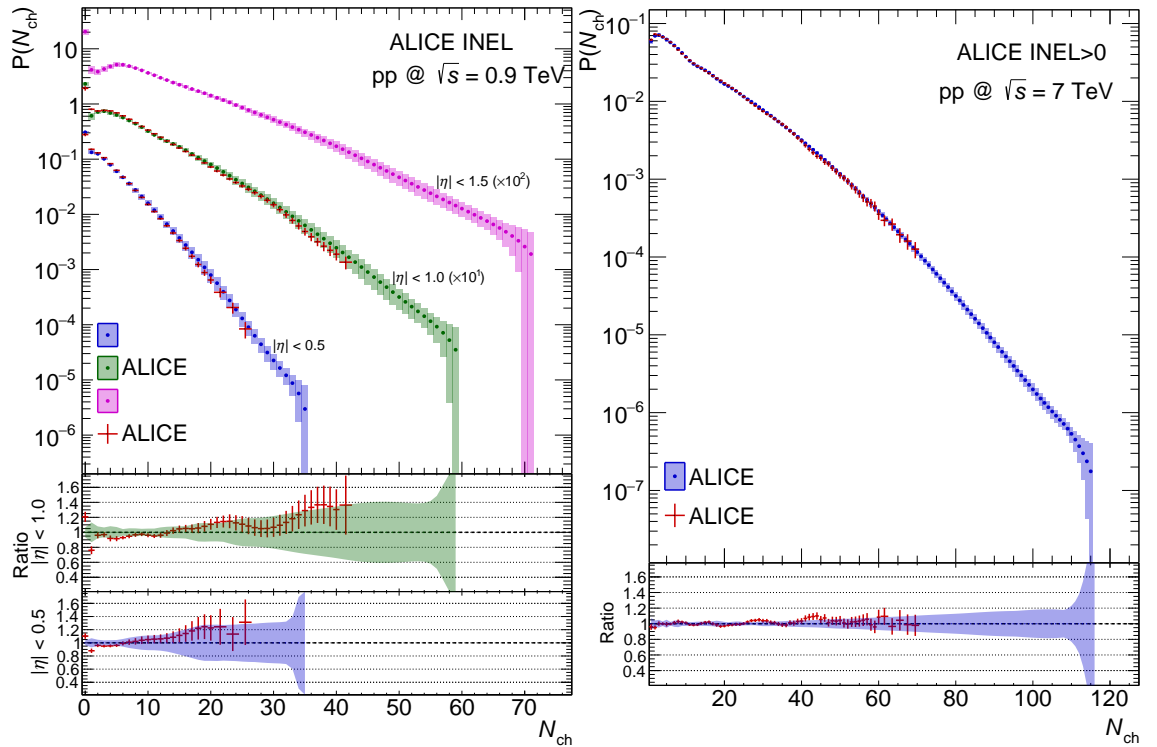


Figure 3.15: Comparison of newly acquired data to previous ALICE measurements. Taken from [2].

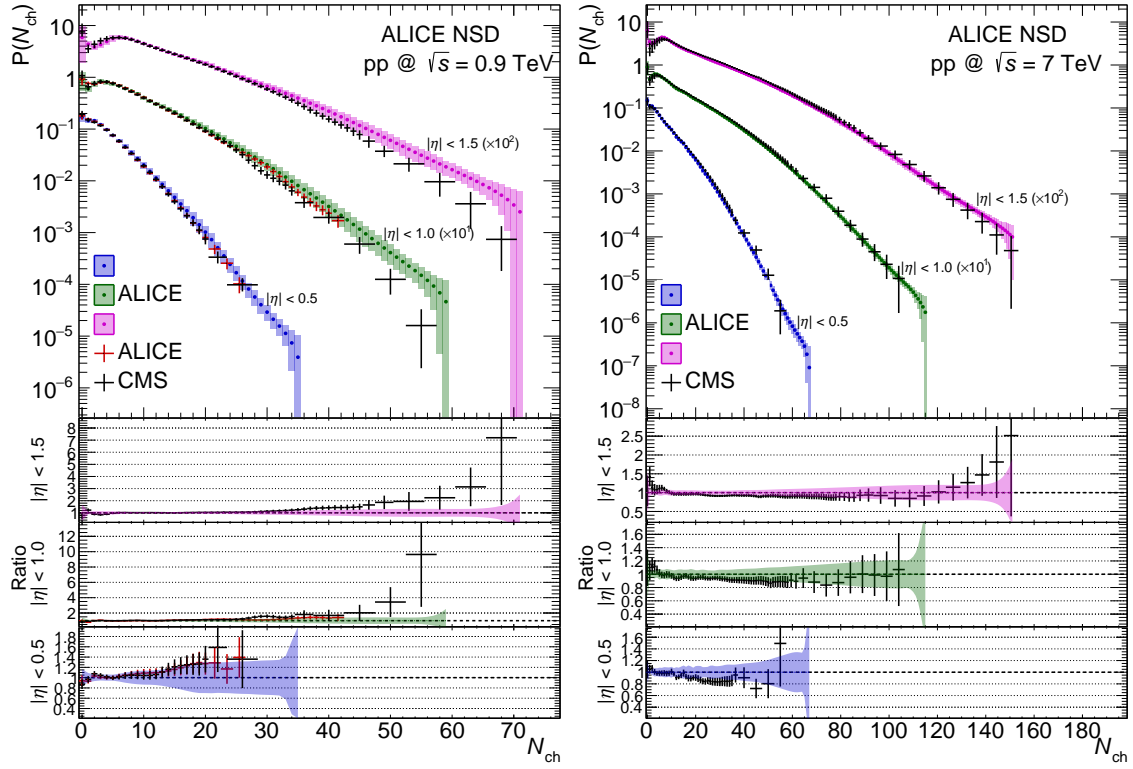


Figure 3.16: Comparison of newly acquired data to previous ALICE and CMS measurements. Taken from [2].

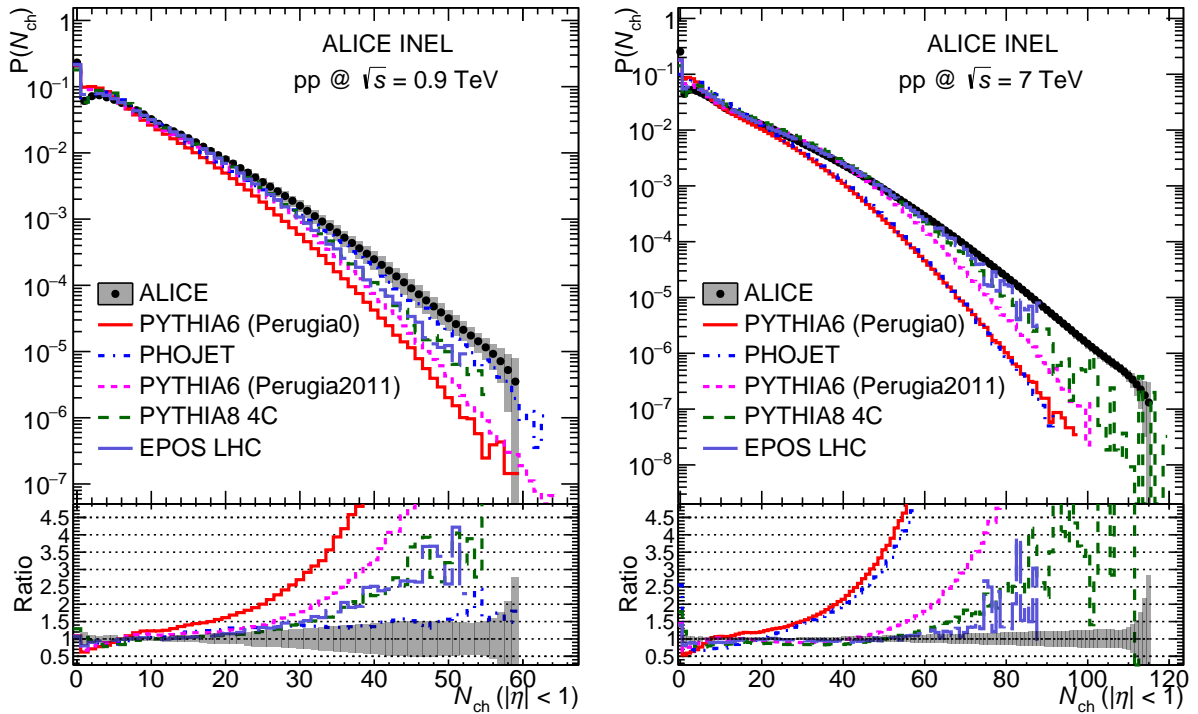


Figure 3.17: Comparison of newly acquired data to data simulated using event generators. Taken from [2].

3.3 Quantum Entanglement

Quantum entanglement is a theoretical phenomenon of quantum physics describing an inner connection between two systems despite their separation in space. This phenomenon cannot be described using classical physics, and it can seemingly create a contradiction with the special theory of relativity.

The actual existence of this contradiction was tested with several experiments. There are numerous theories explaining the phenomenon: one states that relativity is violated and there is a faster than the speed of light information exchange; another one, standardly called the nonlocality, rules that out by stating that those two particles together create one quantum system. The inconsistency of this theory is formulated in the Einstein-Podolsky-Rosen (EPR) paradox.

An experiment testing whether the reality can be described by the local realism rather than quantum mechanics is called a Bell test. It is named after John Stewart Bell, who was able to replace theoretical postulates of locality with a physically realistic condition. All Bell tests performed up to date ruled out the hypothesis of locality and supported the theory of quantum physics [19].

3.3.1 Einstein-Podolski-Rosen paradox

Consider two initially connected quantum systems that are later separated. If a measurement is done on one of those two systems, it should have an immediate effect on the other one. This immediate effect can be investigated at the size scale of a proton using the parton model by Feynman, Bjorken and Gribov by testing the presence of quantum entanglement.

If we take a nucleon in an infinite momentum frame and try to probe it with a virtual photon, the probed parton will be causally disconnected. Still, the rest of the nucleon and the parton create a colour-singlet. Therefore, because of colour confinement, we should be able to encounter quantum entanglement at the subnucleonic scales, where it can be tested.

3.3.2 Testing the presence of quantum entanglement at sub-nucleonic scales

This subsection is based on [20].

Let us consider a collision of two particles, one being a proton and the other either a proton or an electron, and let us name the region of the probed parton A and the rest of the proton B, Fig. 3.18.

If quantum entanglement were present at subnucleonic scales, the entanglement entropy S_E should be equal to the Boltzmann entropy S_B . So the tested relation is:

$$S_E = S_B. \tag{3.5}$$

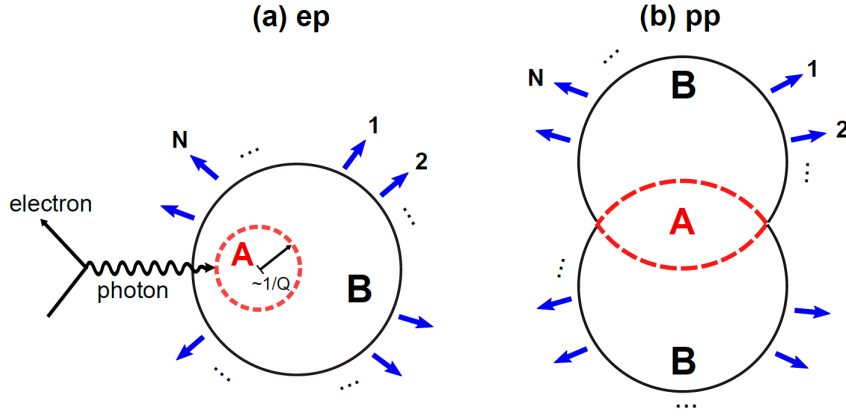


Figure 3.18: Schemes of: a) electron-proton deeply inelastic scattering, b) proton-proton inelastic collision. Taken from [20].

The entanglement entropy is the von Neumann entropy resulting from the quantum entanglement between regions A and B.

The von Neumann entropy is the Gibbs entropy from classical mechanics transformed into quantum mechanics, and it can be calculated from the initial-state parton distribution. We focus only on small fractions of the proton's momentum carried by the parton, denoted x , so the gluons strongly dominate, and the entanglement entropy can be approximated as

$$S_E = \ln(xG(x)), \quad (3.6)$$

where $G(x)$ is the gluon distribution.

The Boltzmann entropy, on the other hand, can be reconstructed from the multiplicity distribution of final-state hadrons $P(N)$, where $P(N)$ is the probability of multiplicity being equal to N :

$$S_B = - \sum P(N) \ln(P(N)). \quad (3.7)$$

The von Neumann entropy S_E is the entropy created by the entanglement between A and B, whereas the Boltzmann entropy is the entropy created by the entanglement between B and A. As the situation is symmetric, the entropies have to be the same. Hence the relation $S_E = S_B$.

3.3.2.1 Test using simulated data

The simplest way to test this relation would be in electron-proton deep-inelastic scattering (DIS). Nonetheless, data measured with HERA did not cover the needed region of $x < 10^{-3}$. So simulated data had to be used. However, none of the simulation generators contain entanglement. That unsurprisingly resulted in a violation of the wanted relation, which can be seen for Pythia 6 in Fig. 3.19. For higher virtuality, the discrepancy gets even bigger.

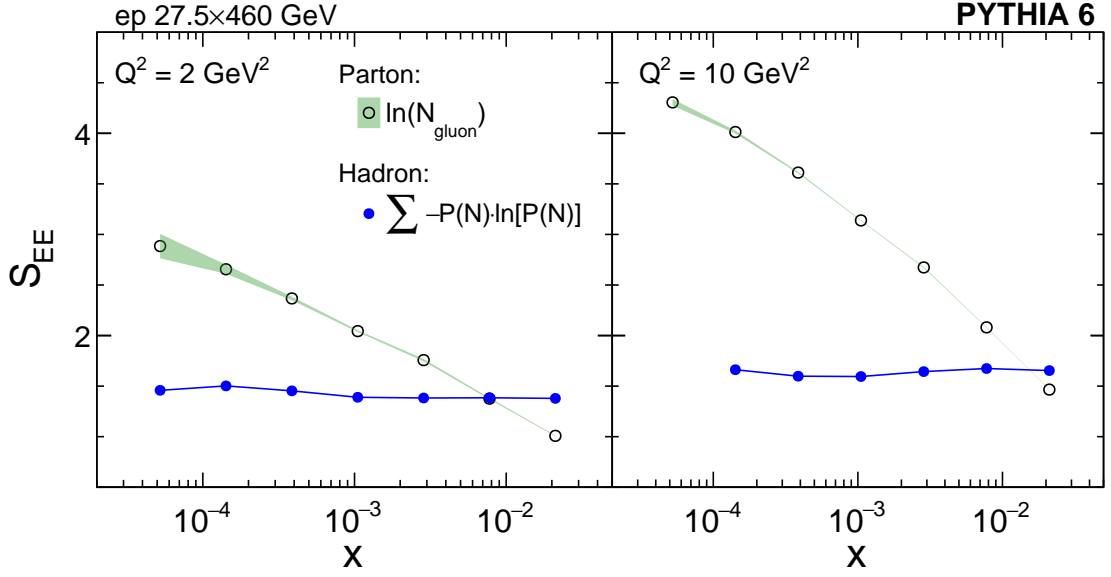


Figure 3.19: Boltzmann and von Neumann entropies, for virtualities $Q^2 = 2$ and 10 GeV^2 , calculated from the generated final-state multiplicity distributions depicted by the blue dots and from the generated gluon distribution depicted by the green band, respectively. Taken from [20].

3.3.2.2 Test using experimental data

The theory has been successfully tested using CMS data from proton-proton collisions, and the results are consistent with ATLAS and ALICE measurements for the same pseudorapidity ranges.

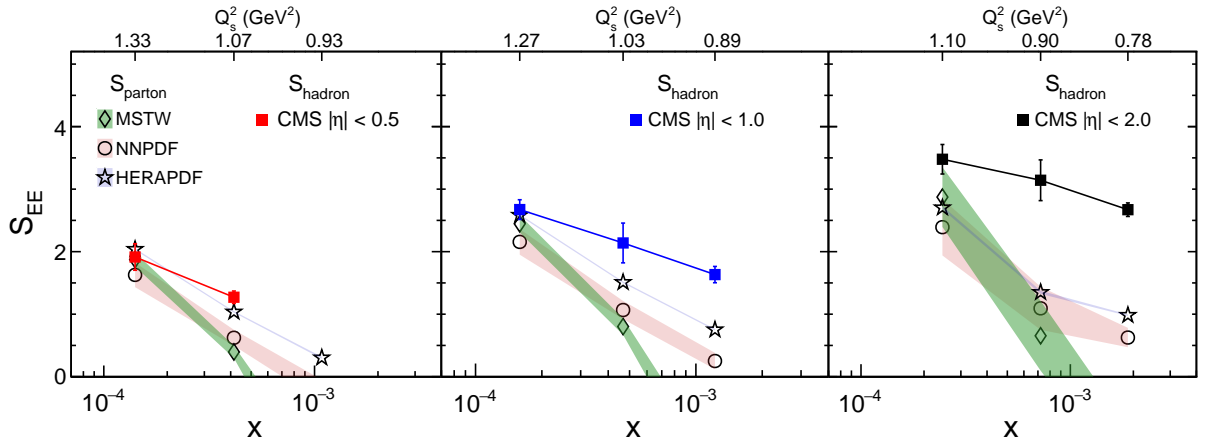


Figure 3.20: Boltzmann entropy, computed from the final-state multiplicity distributions measured by CMS, and the von Neumann entropies, calculated from the initiate-state gluon distributions using three parton distribution functions, for each of the three pseudorapidity ranges. Taken from [20].

In Fig. 3.20, the Boltzmann entropy, computed from the final-state multiplicity distributions measured by CMS, and the von Neumann entropies, calculated from the initiate-state gluon distributions using three different parton distribution functions, for three pseudorapidity ranges: $|\eta| = 0.5, 1.0, \text{ and } 2.0$, are shown. The correspondence between the two entropies gets lower with a wider pseudorapidity range, but the relation seems to hold approximately.

According to [20], "this observation provides a strong direct indication of quantum entanglement at subnucleonic scales".

Chapter 4

Analysis of the first pilot beam data in Run 3

The primary focus of the experimental part of this thesis was to produce simulated data of multiplicity measurements in proton-proton collisions done by the ALICE detector using the new O² software. After a successful installation of the mentioned software, I was able to produce thousands of events.

During the time I spent on simulations, the first real data were obtained with ALICE during a test run in September 2021. Two runs with the different polarity of the L3 magnet were analysed. These runs were taken at center-of-mass energy equal to the injection energy, $\sqrt{s} = 0.9$ TeV. A simple analysis of these data is the focus of this chapter.

The analysed data were acquired to calibrate the detectors and the new software. It is a work in progress. Therefore, the analysis does not produce final results or definite answers. The analysis was carried out entirely within the O² framework. I started with an example code by Anton Alkin; then, I modified and extended this code to perform my analysis. The code was run locally on my computer (no use of the hyper loop system) after downloading the AO2D files of these runs. I used the `apass2` reconstruction.

The structure of this chapter is the following. Firstly, the event selection used is explained in Section 4.1, the vertex distribution is discussed in Section 4.2. Next, the difference between positively and negatively charged particles is investigated in Section 4.3. The distribution of momenta is shown in Section 4.4 and the multiplicity distribution is presented in Section 4.5. Finally, in Section 4.6 the measured data are compared with Monte Carlo simulations.

4.1 Selection

During the test runs, no special focusing of the beams was done, yet many events were still detected. In total, almost $28 \cdot 10^5$ events were detected in the run 505582 with the negative polarity of the L3 magnet, later in this text called only 582, and

nearly $39 \cdot 10^5$ events in the run 505673 with positive polarity, later in this text called only 673.

Normalised data selection for both runs is in Fig. 4.1. The normalisation is the inverse of the number of events analysed in the given run. The last three sections (good bunch-crossings, bunch-crossings with collisions and bunch-crossings with pile-up/splitting) are empty because the data analysis is still in progress, and these factors have not been investigated yet.

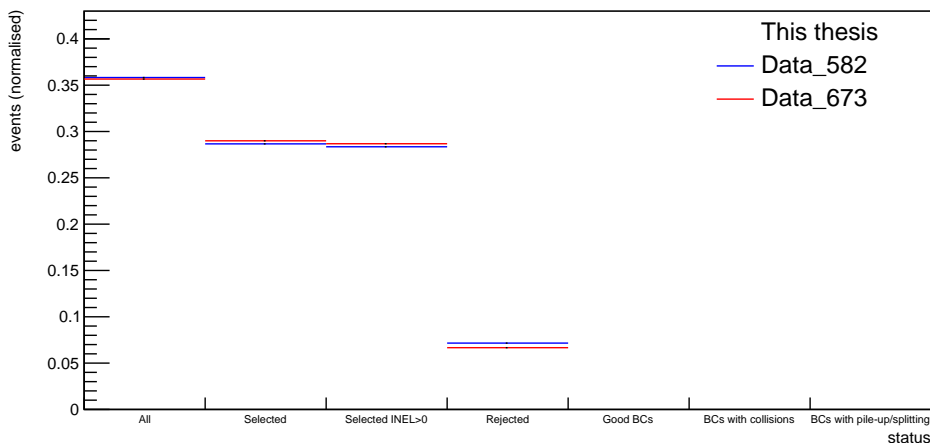


Figure 4.1: Normalised data selection for both runs. BC means bunch-crossing.

4.2 Reconstructed vertex

The efficiency of the vertex reconstruction is dependent on the position of the vertex and the multiplicity of a given event. However, the exact efficiency is yet to be determined. The vertex position distribution along the z axis is shown in Fig. 4.2.

There is no visible difference in the vertex positioning between the two polarities. The only difference between the two graphs in Fig. 4.2 is that there is a higher density of events in the run 673 with positive polarity, which is caused by the fact that there were more events detected.

4.3 Charge of particles

The normalised number of positively and negatively charged particles detected is shown in Fig. 4.3. It is seen that there are slightly more negatively charged particles in the run 582 with the negative polarity of the L3 magnet. I do not understand this behaviour yet.

For run 673, the sum of the normalised numbers does not give a 1. This might be caused by a wrongly done normalisation or by doing the normalisation with the rejected events also accounted for. The real reason is currently under investigation.

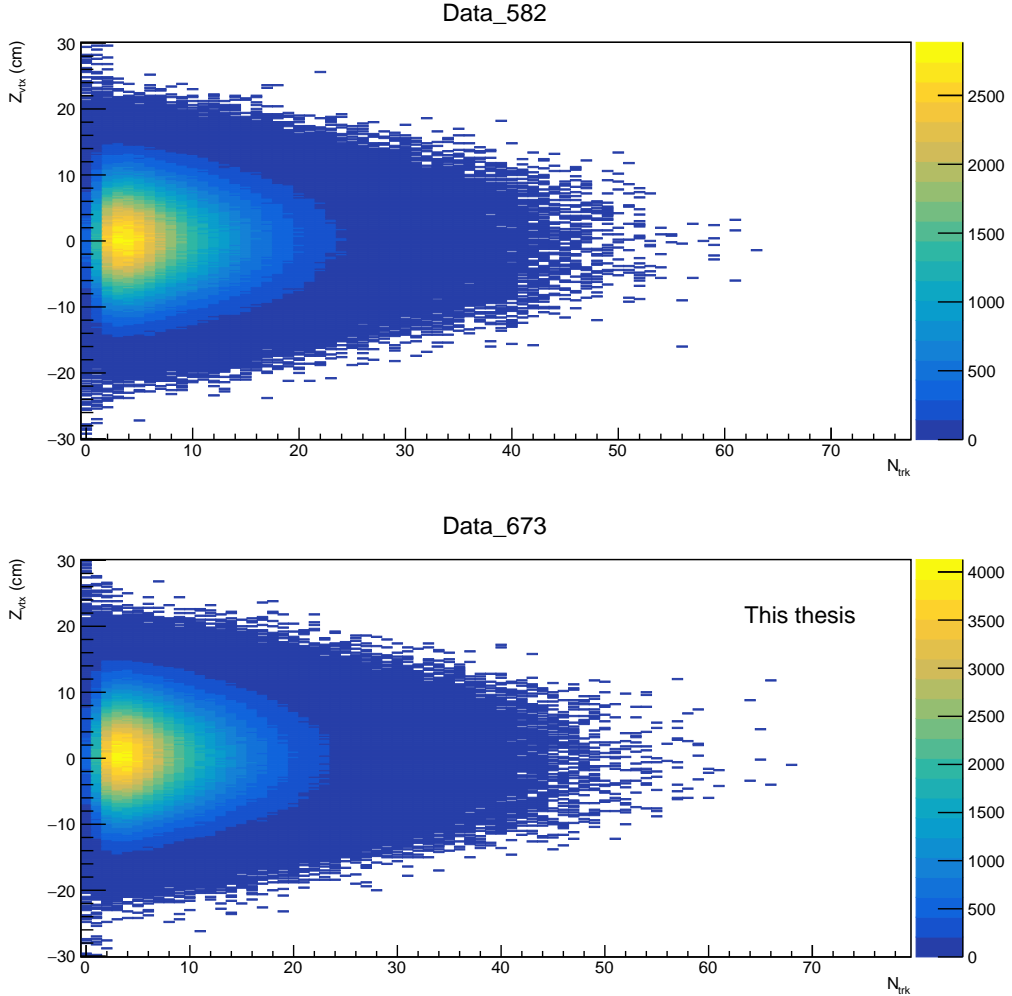


Figure 4.2: The vertex position distribution along the z axis in the run 582 with the negative polarity of the L3 magnet (upper panel) and the run 673 with the positive polarity of the L3 magnet (lower panel).

4.3.1 φ, η distribution

The φ, η distribution of all detected particles is shown in Fig. 4.5. The differences between the two polarities of the L3 magnet are small and due to statistical fluctuations. The difference in intensity is again caused by a higher number of events in run 673 than in run 582. The gap in the φ region between 4 and 5 was caused by a detector deficiency.

The ITS layers are composed of so-called staves, as shown in Fig. 4.4. The innermost layer has 12, and each next has a few more than the one before. The outermost layer has 48 staves. During the test run, one stave in layer 5 had a problem with flash memory and was off. Moreover, one stave in layer 4 and one in layer 5 had alignment issues, and their measurements were inconclusive [21].

In Fig. 4.6 and Fig. 4.7 are shown separately the φ, η distributions for the run 582 and 673, respectively. The distributions show a wider pseudorapidity range for

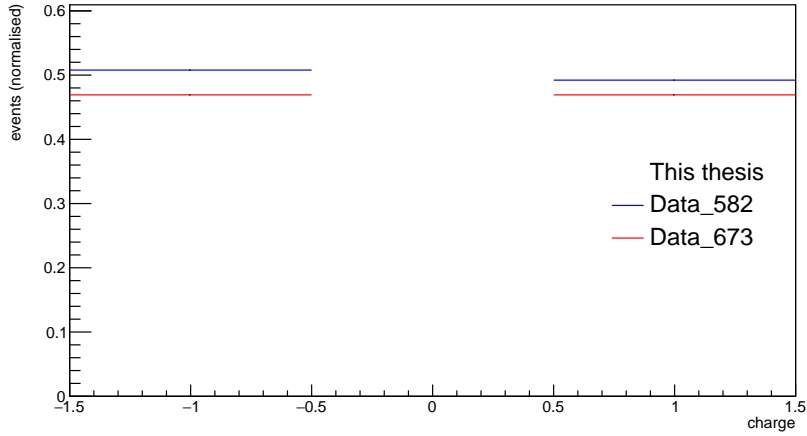


Figure 4.3: The normalised number of positively and negatively charged particles in run 582 with negative polarity of the L3 magnet and in run 673 with positive polarity of the L3 magnet.

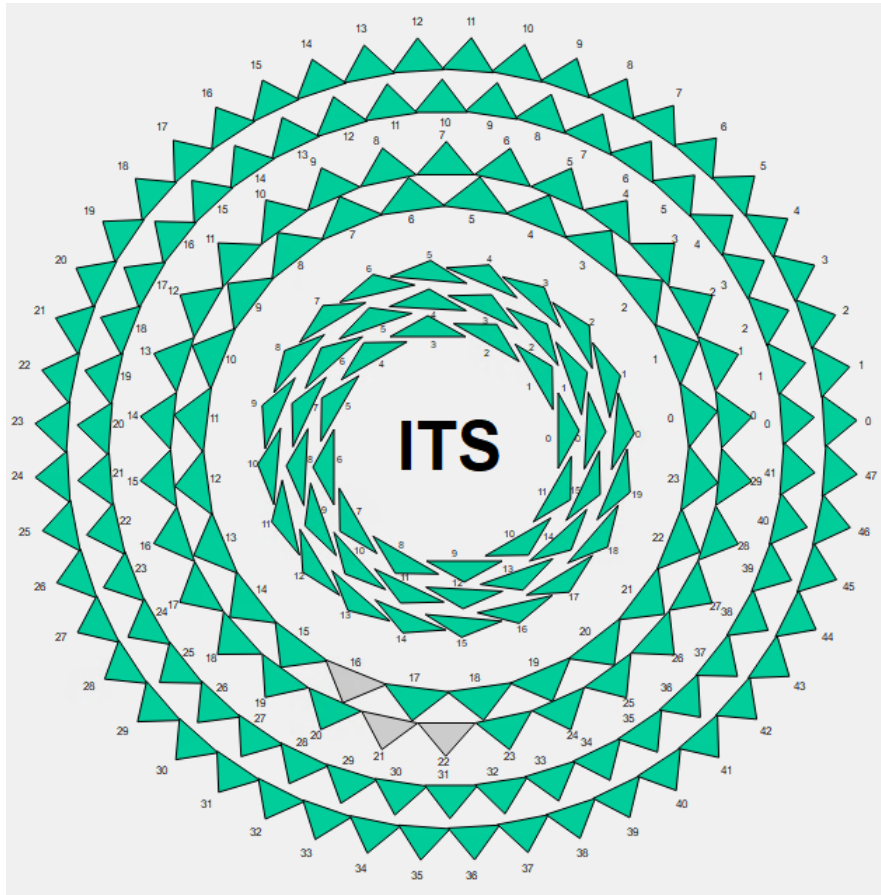


Figure 4.4: The ITS structure with marked staves, which were deficient during the test runs in September 2021. Taken from [21].

positive particles in the run 582 and negative particles for the run 673 in the φ region between 3 and 4 and between 0 and 1. This is basically compensated by a lower

pseudorapidity range of the particles with the opposite charge, creating a more or less uniform range of all particles, which is expected. These fluctuations were also caused by detector deficiency.

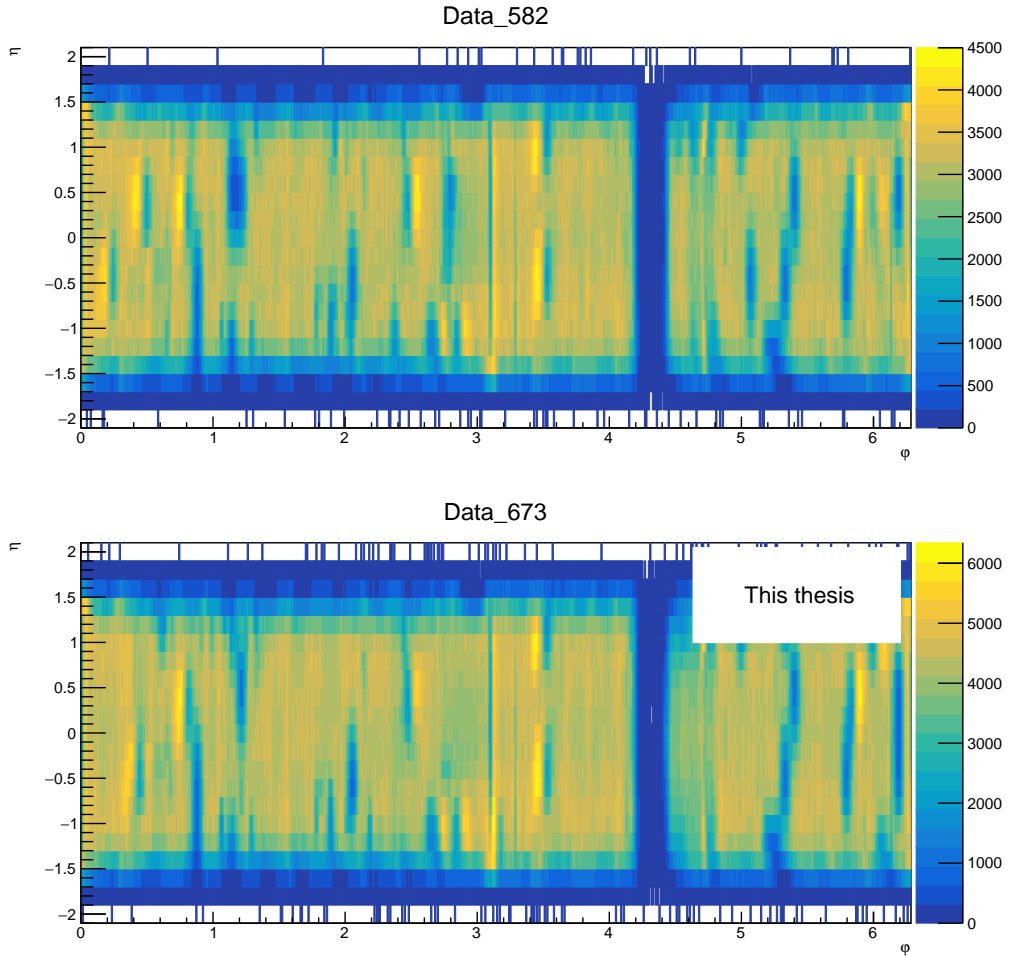


Figure 4.5: The φ, η distribution of detected particles in the run 582 with the negative polarity of the L3 magnet (upper panel) and the run 673 with the positive polarity of the L3 magnet (lower panel).

4.4 Transverse momenta

The measured transverse momenta distributions are shown in Figs 4.8, and 4.9; they follow the expected distributions. The only deviations occur around $p_T = 0.1 \text{ GeV}/c$ for positively charged particles in the run 673 with the negative polarity of the L3 magnet and for negatively charged particles in the run 582 with the positive polarity of the L3 magnet. The reason is still being investigated.

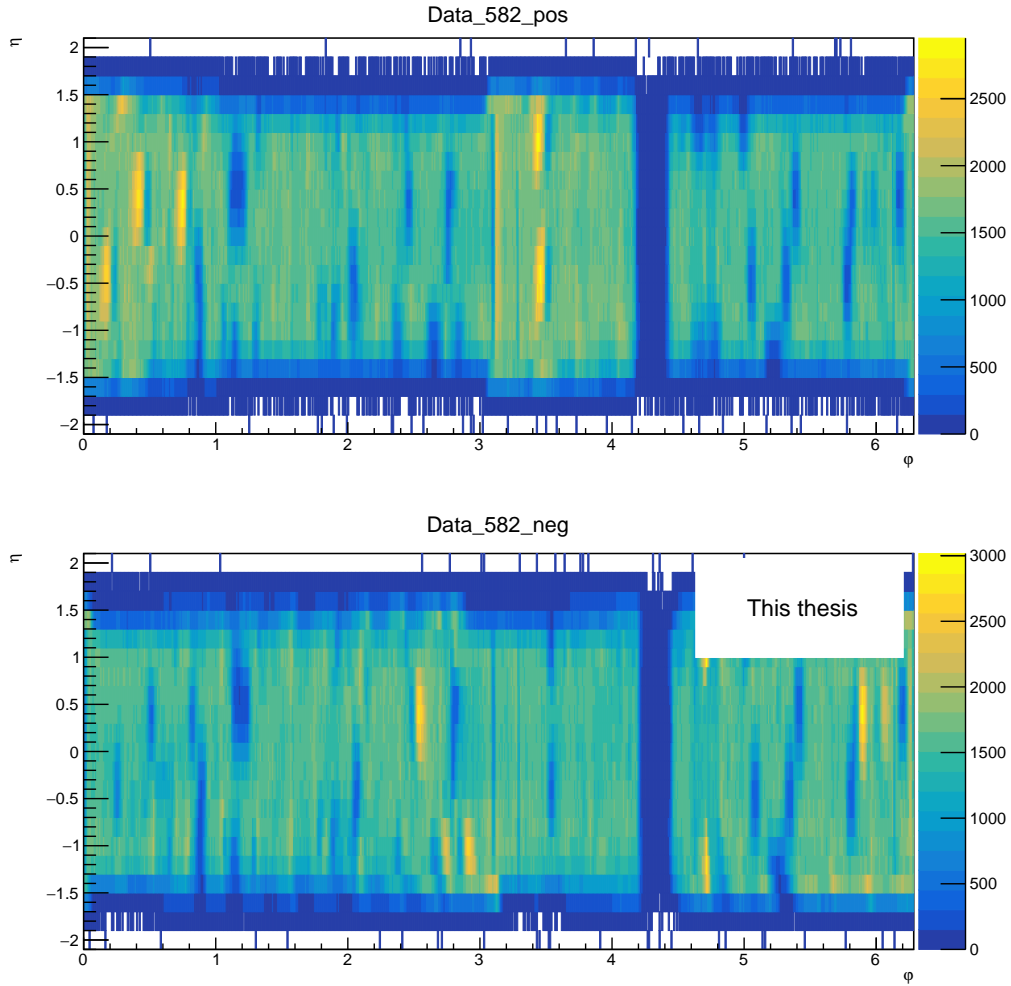


Figure 4.6: The φ, η distribution of detected particles in the run 582 with the negative polarity of the L3 magnet for positively (upper panel) and negatively (lower panel) charged particles.

4.5 Multiplicity

As mentioned in the first chapter, measurements of multiplicity are direct and need a minimum of external information. Acquiring the multiplicity of a given event is fast, and the results can be directly compared to previous or simulated data. Therefore, it is the perfect validation tool for the new detectors and software.

As expected, the number of events decreases with increasing multiplicity. The multiplicity distribution is almost the same for both studied runs, which was anticipated. Normalised multiplicity distributions for runs 582 and 673 are in Fig. 4.10.

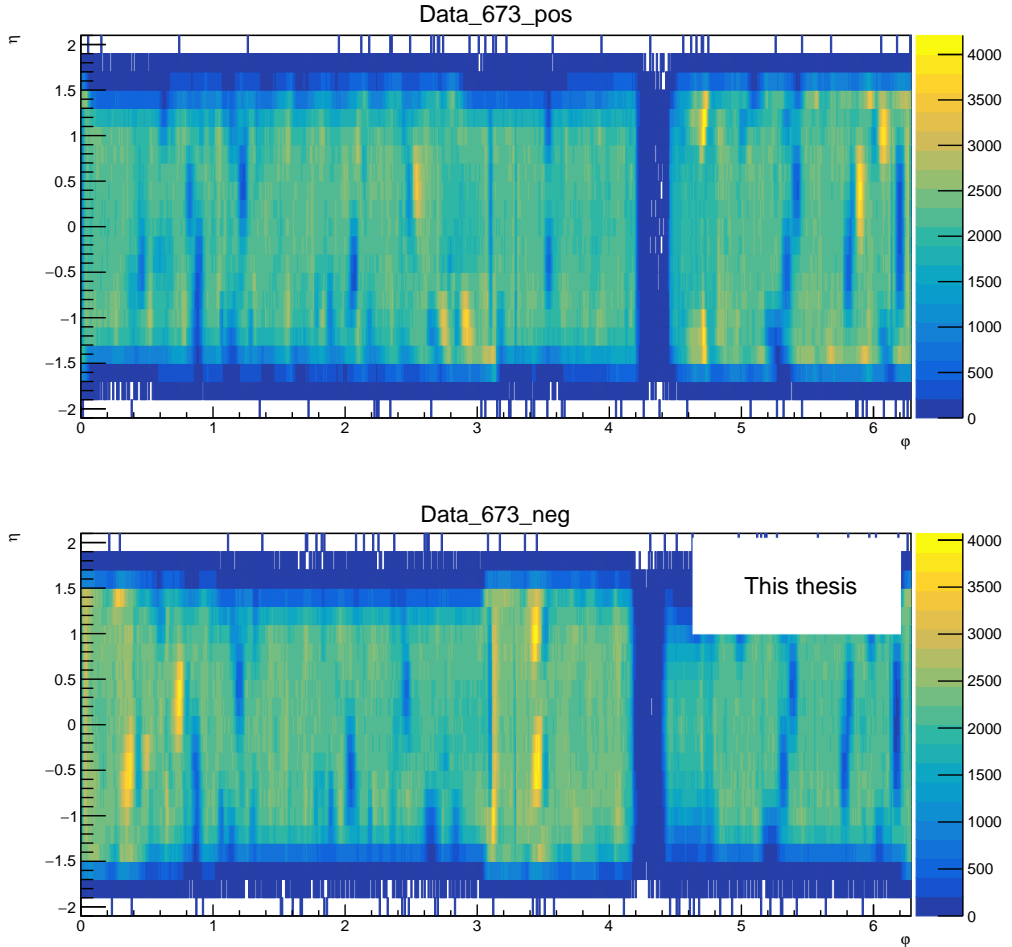


Figure 4.7: The φ, η distribution of detected particles in the run 673 with the negative polarity of the L3 magnet for positively (upper panel) and negatively (lower panel) charged particles.

4.6 Comparison with MC simulation

Data simulated with a Monte Carlo generator (PYTHIA 6, official ALICE production, tag LHC21i1_nightly, run number 301120) are consistent with the measurements. There were only $0.84 \cdot 10^5$ events, and, as can be seen in Fig. 4.11, more than a third of those events were rejected. The vertex position distribution, shown in Fig. 4.14, tallies with the recorded data. The same applies to the distributions of transverse momentum (although the feature at $p_T = 0.1$ GeV/ c is not seen in MC) and multiplicity, which can be seen in Fig. 4.15 and Fig. 4.13, respectively. The numbers of positively and negatively charged particles in the simulated data are more evenly distributed than in the data.

The φ, η distribution of the simulated data, shown in Fig. 4.16, differs from the measured ones because of the detector deficiency. The blue gap around $\varphi = 3.1$ is caused by the misalignment of the ITS staves. This misalignment is also slightly visible in the real data. This shifted structure has been added to the recent simulations to

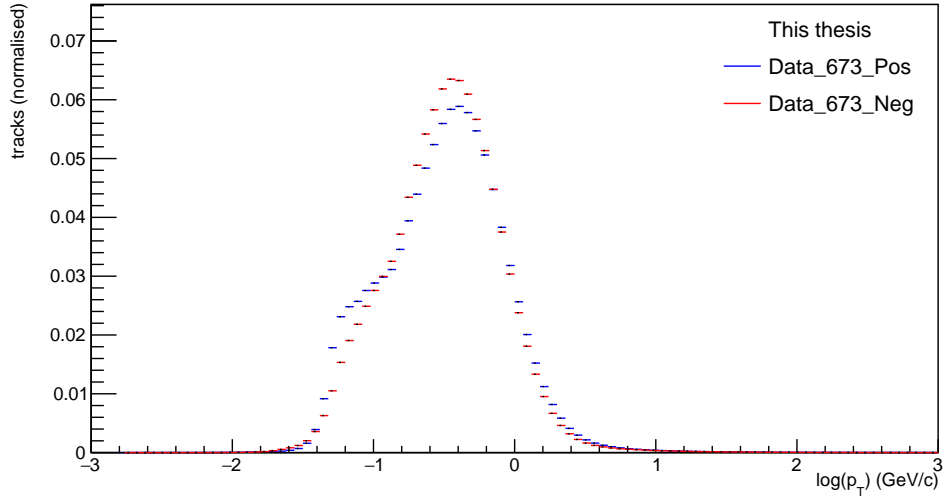


Figure 4.8: The transverse momentum distribution with the logarithmic x axis of the run 673 with the negative polarity of the L3 magnet.

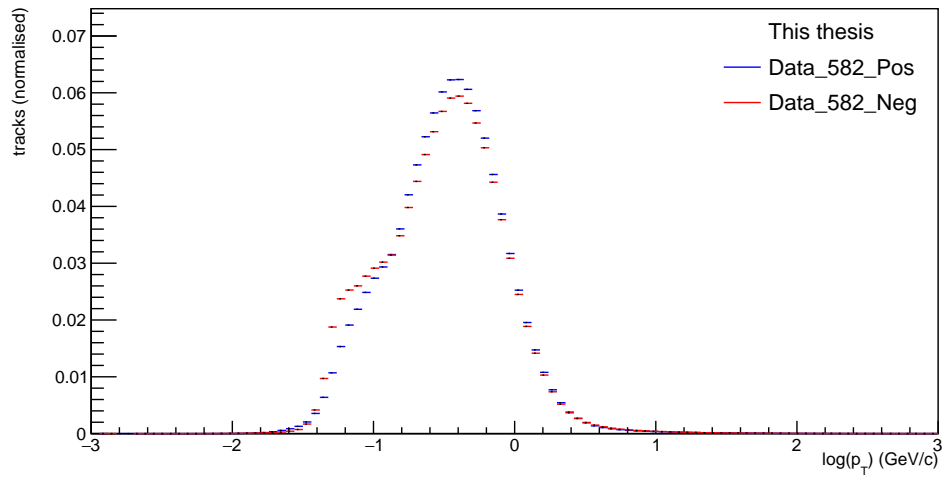


Figure 4.9: The transverse momentum distribution with the logarithmic x axis of the run 582 with the positive polarity of the L3 magnet.

calibrate the ITS correctly.

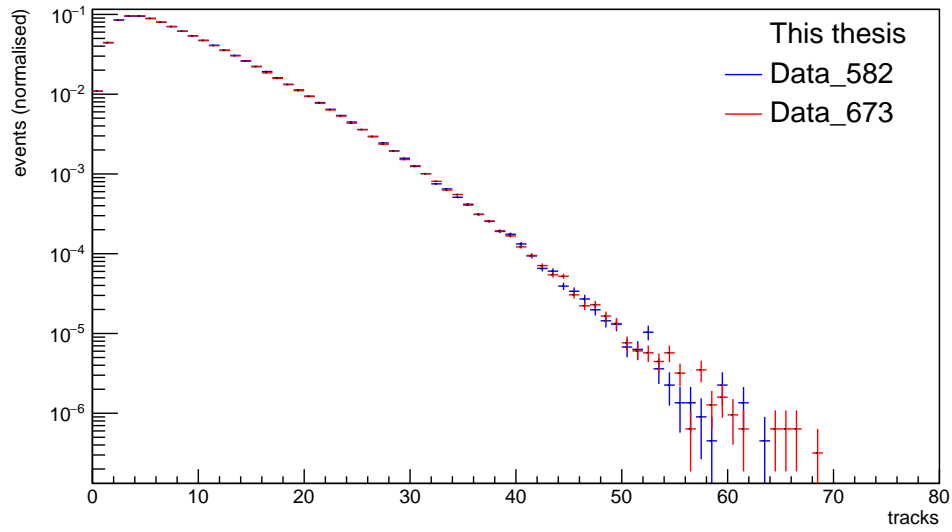


Figure 4.10: Normalised multiplicity distributions for run 582 with negative polarity of the L3 magnet and run 673 with positive polarity of the L3 magnet.

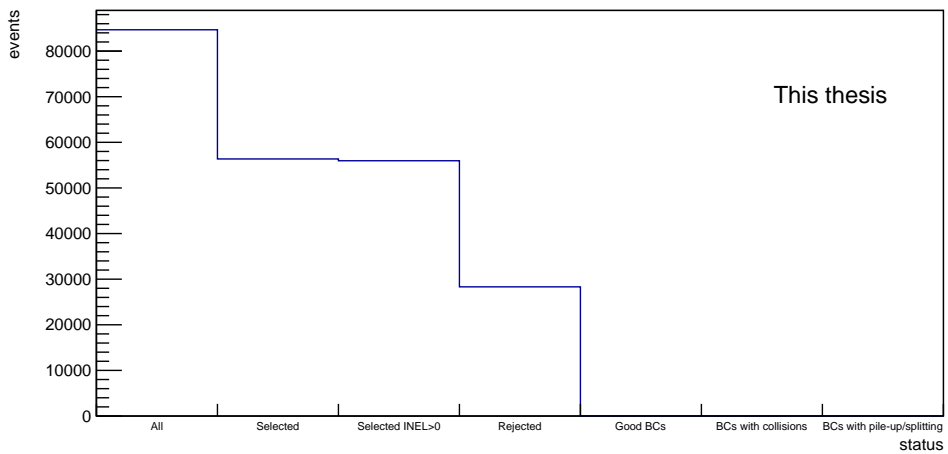


Figure 4.11: Data selection of Monte Carlo simulations. BC means bunch-crossing.

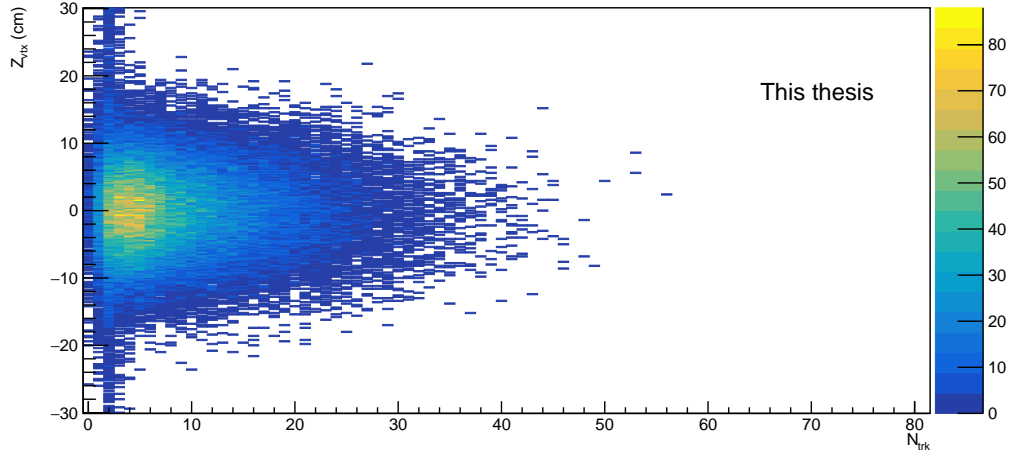


Figure 4.12: The vertex position distribution along the z axis of the Monte Carlo simulated data.

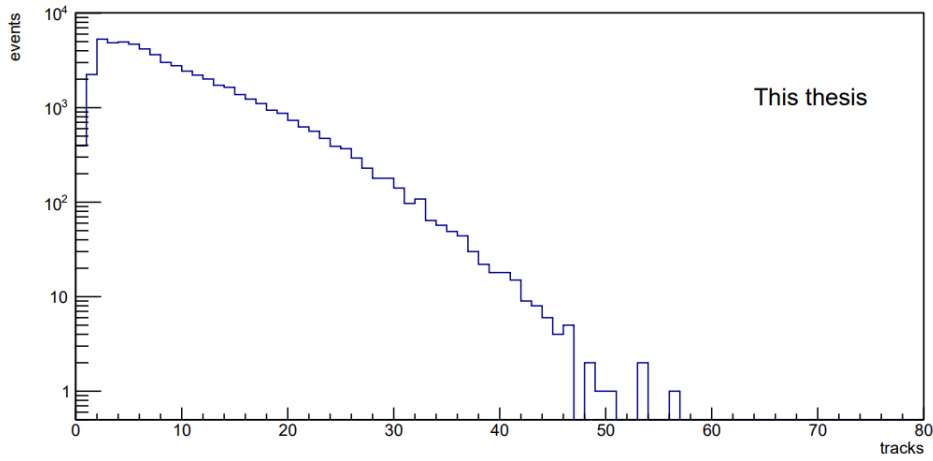


Figure 4.13: Multiplicity distribution of Monte Carlo simulated data.

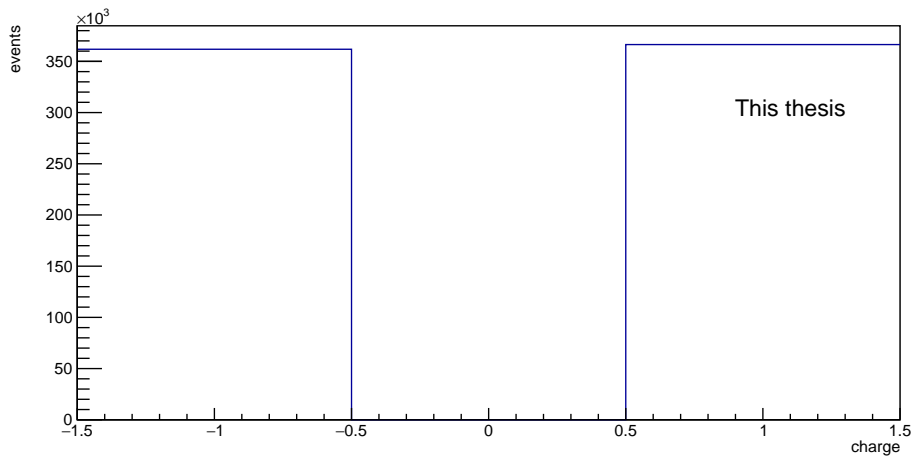


Figure 4.14: Number of positively and negatively charged particles in the Monte Carlo simulated data.

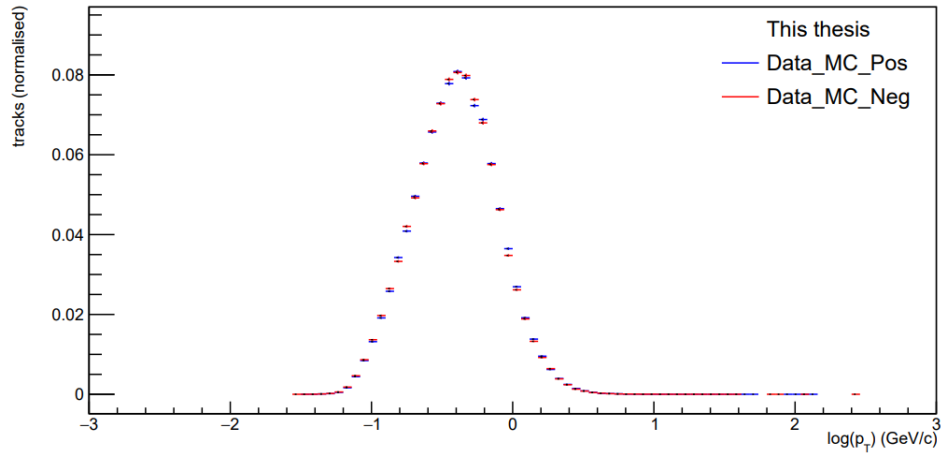


Figure 4.15: The transverse momentum distribution with the logarithmic x axis of the Monte Carlo simulated data.

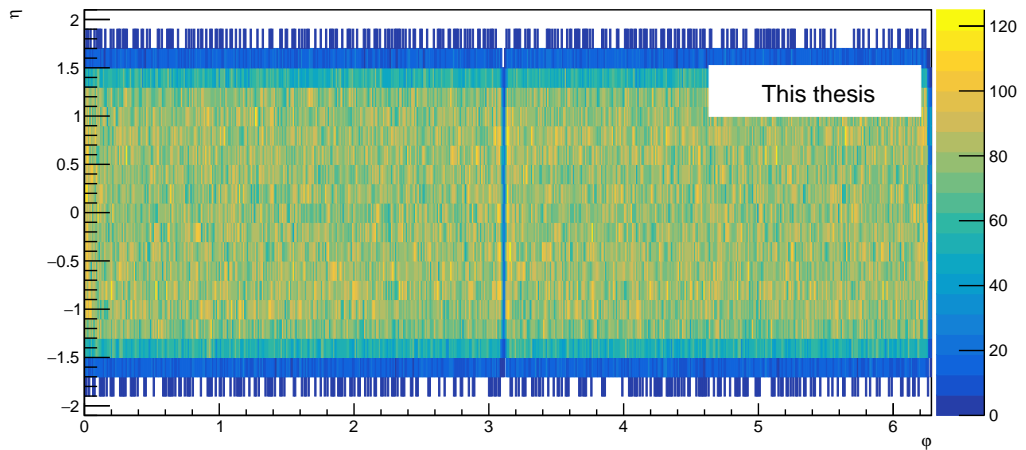


Figure 4.16: φ, η distribution of detected particles in the Monte Carlo simulated data.

Summary

The theoretical part of this thesis contains a simple presentation of the Standard Model theory, the description of the structure and workings of the LHC and the ALICE experiment, and their upgrade during the last Long Shutdown. Chapter 1 consists of the introduction of elementary particles, the four fundamental forces, and the terminology and principles used later in this thesis. To the LHC and ALICE is dedicated Chapter 2. In addition, some of the previous multiplicity measurements in proton-proton collisions are discussed in Chapter 3. This chapter also explains the use of multiplicity in quantum entanglement testing. It is shown there that the presence of quantum entanglement at the subnucleonic scales could be explored by analyzing the data from proton-proton collisions.

Chapter 4 contains my contribution to the analysis of the first data collected during Run 3. These data are only from the test runs, which serve for calibration and for corrections of the new detectors and the new software. The data analysis is a work in progress. Thus no final results have been yet produced. This thesis provides a comparison of two runs with different polarities of the L3 magnet. The expected symmetry between the negatively and positively charged particles and between the two runs is shown and proved. A deficiency of the ITS detector is visible in the φ, η distributions of both investigated runs.

First, the data selection shows that about one fifth of the events was rejected. The distribution of events regarding bunch-crossing conditions is yet to be created. Second, the vertex positioning on the z axis is shown for both runs with no significant differences. The same applies to the φ, η , momentum, and multiplicity distributions. From the φ, η distributions, it is evident that some detector deficiency has occurred. This deficiency was identified as a problem with three ITS staves. An ITS team has already brought them back into operation. The fractions of negatively and positively charged particles were also compared. The reason, why the total normalised number of detected particles in the run 505673 is not one, is currently under study.

Furthermore, Monte Carlo simulated data were also analysed, and the results are consistent with the measured data. The only significant difference is in the φ, η distribution because the simulated ITS had no deficiencies. However, the simulations do contain the misalignment of the ITS staves, creating a gap around $\varphi = 3.1$.

To conclude, I learned how to use the new ITS framework to do the analysis. I also modified and extended existed workflow and used it to study real and simulated data from the September pilot beam tests. All the analysed data correspond with our expectations. One problem with the ITS is seen in the data. The ITS team

corrected it. On the whole, the runs 505673 and 505582 with the different polarities of the L3 magnet show all the expected symmetries between positive and negative particles.

New pilot beam data were taken in June 2022 (when this thesis was written). The new data show the ITS inefficiencies are corrected. Data at the largest energy to date will be taken in the following months. From these data, a measurement of the charged-particle multiplicity will be performed, not only using the ITS as in this thesis but also the new MFT detector. Later on, new data in lead-lead collisions will be recorded, allowing the ALICE Collaboration to perform new and more precise multiplicity measurements using the new ITS and MFT detectors. The tools developed in this thesis and the experience gained in this first analysis will be very useful in studying the new data.

Bibliography

- [1] “First proton-proton collisions at the LHC as observed with the ALICE detector: measurement of the charged-particle pseudorapidity density at $\sqrt{s} = 900$ GeV”. In: *The European Physical Journal C* 65.1-2 (Dec. 2009), pp. 111–125. DOI: 10.1140/epjc/s10052-009-1227-4. URL: <https://doi.org/10.1140%2Fepjc%2Fs10052-009-1227-4>.
- [2] “Charged-particle multiplicities in proton-proton collisions at $\sqrt{s} = 0.9$ to 8 TeV”. In: *The European Physical Journal C* 77.1 (Jan. 2017). DOI: 10.1140/epjc/s10052-016-4571-1. URL: <https://doi.org/10.1140%2Fepjc%2Fs10052-016-4571-1>.
- [3] The Editors of Encyclopaedia. *Electron*. 2019. URL: <https://www.britannica.com/science/electron>.
- [4] Jerome I. Friedman. “Deep inelastic scattering: Comparisons with the quark model”. In: *Rev. Mod. Phys.* 63 (1991), pp. 615–629. DOI: 10.1103/RevModPhys.63.615.
- [5] *File:Standard Model of Elementary Particles Anti.svg*. 2018. URL: https://commons.wikimedia.org/wiki/File:Standard_Model_of_Elementary_Particles_Anti.svg.
- [6] Moustapha Thioye. “Topics in the measurement of electrons with the ATLAS detector at the LHC”. Presented on 25 Mar 2008. 2008. URL: <https://cds.cern.ch/record/1120327>.
- [7] *Convention for the establishment of a European organization for nuclear research: Paris, 1st July, 1953: as amended. Convention pour l'établissement d'une Organisation européenne pour la Recherche nucléaire. Paris, le 1er juillet 1953 : telle qu'elle a été modifiée*. Geneva: CERN, 1971. URL: <https://cds.cern.ch/record/330625>.
- [8] Chris Llewellyn Smith. “Genesis of the Large Hadron Collider”. In: *Philosophical Transactions of the Royal Society A* (2015).
- [9] Esma Mobs. *The CERN accelerator complex - August 2018. Complexe des accélérateurs du CERN - Août 2018*. General Photo. Aug. 2018. URL: <https://cds.cern.ch/record/2636343>.
- [10] *A Large Ion Collider Experiment*. 2022. URL: <https://alice-collaboration.web.cern.ch/>.
- [11] *ALICE*. 2022. URL: <https://home.cern/science/experiments/alice>.

- [12] Arturo Tauro. “ALICE Schematics”. General Photo. May 2017. URL: <https://cds.cern.ch/record/2263642>.
- [13] “The upgrade of the ALICE TPC with GEMs and continuous readout”. In: *JINST* 16 (Dec. 2020). 88 pages, 60 figures, P03022. 87 p. DOI: 10.1088/1748-0221/16/03/P03022. arXiv: 2012.09518. URL: <https://cds.cern.ch/record/2758225>.
- [14] *ALICE forward detectors: FMD, TO and VO: Technical Design Report*. Technical design report. ALICE. Submitted on 10 Sep 2004. Geneva: CERN, 2004. URL: <http://cds.cern.ch/record/781854>.
- [15] Maciej Slupecki. “The Fast Interaction Trigger for the ALICE Upgrade”. dissertation. University of Jyväskylä, 2020.
- [16] *Technical Design Report for the Muon Forward Tracker*. Tech. rep. Jan. 2015. URL: <https://cds.cern.ch/record/1981898>.
- [17] Eulisse, Giulio et al. “Evolution of the ALICE Software Framework for Run 3”. In: *EPJ Web Conf.* 214 (2019), p. 05010. DOI: 10.1051/epjconf/201921405010. URL: <https://doi.org/10.1051/epjconf/201921405010>.
- [18] R Schmidt. “Beam-beam observations in the SPS proton antiproton collider”. In: *Part. Accel.* 50 (1995), pp. 47–60. URL: <https://cds.cern.ch/record/304824>.
- [19] John F. Clauser et al. “Proposed Experiment to Test Local Hidden-Variable Theories”. In: *Phys. Rev. Lett.* 23 (15 Oct. 1969), pp. 880–884. DOI: 10.1103/PhysRevLett.23.880. URL: <https://link.aps.org/doi/10.1103/PhysRevLett.23.880>.
- [20] Zhoudunming Tu, Dmitri E. Kharzeev, and Thomas Ullrich. “Einstein-Podolsky-Rosen Paradox and Quantum Entanglement at Subnucleonic Scales”. In: *Phys. Rev. Lett.* 124 (6 Feb. 2020), p. 062001. DOI: 10.1103/PhysRevLett.124.062001. URL: <https://link.aps.org/doi/10.1103/PhysRevLett.124.062001>.
- [21] Jian Liu. *ITS pilot beam test and upcoming plans*. RC meeting. 9/11/2021.